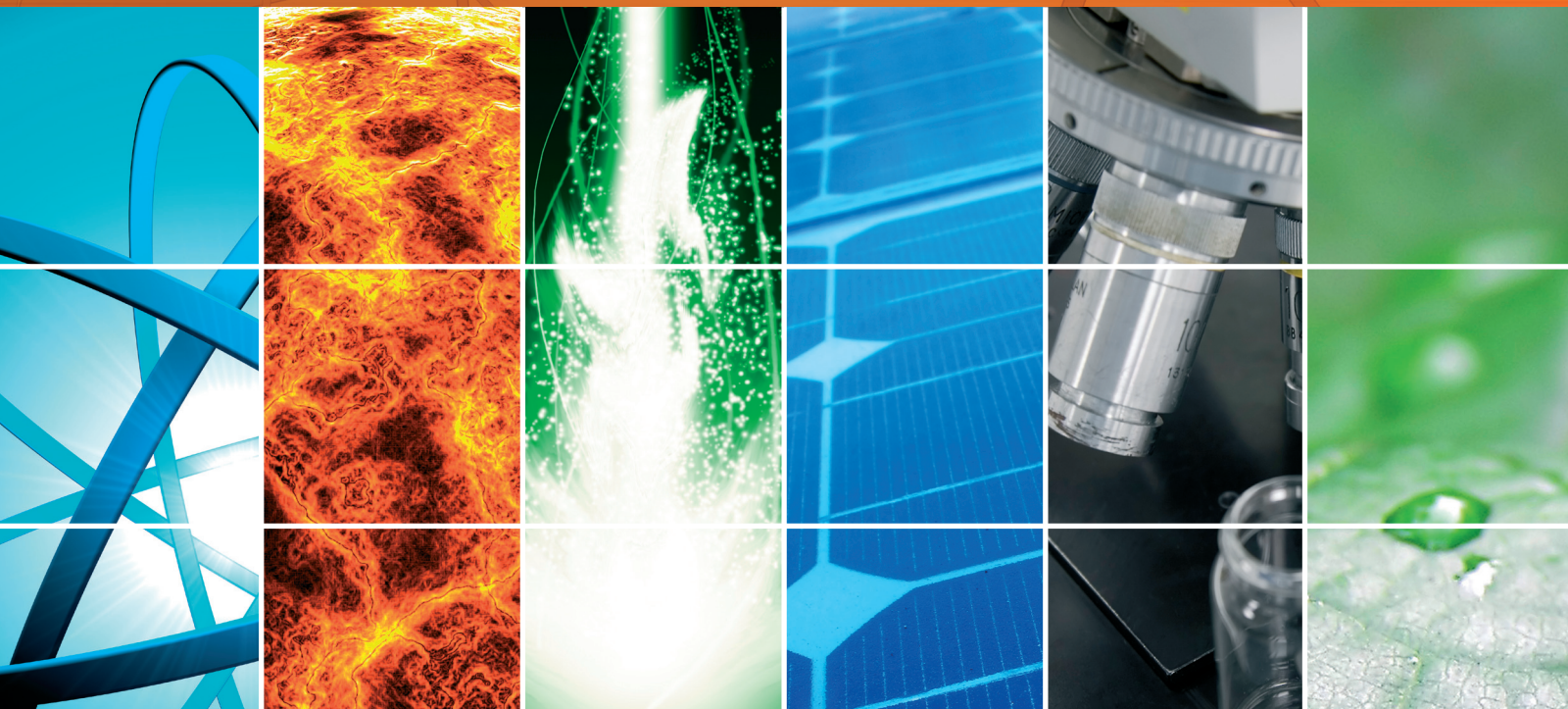


Prompt and Delayed Fluorescences

Guest Editors: Fuat Bayrakceken, Necdet Aslan, Ş. ipek Karaaslan,
Korkut Yegin, J. R. Lombardi, and Aydogan Ozcan





Prompt and Delayed Fluorescences

International Journal of Photoenergy

Prompt and Delayed Fluorescences

Guest Editors: Fuat Bayrakceken, Necdet Aslan,
Ş. İpek Karaaslan, Korkut Yegin, J. R. Lombardi,
and Aydogan Ozcan



Copyright © 2012 Hindawi Publishing Corporation. All rights reserved.

This is a special issue published in "International Journal of Photoenergy." All articles are open access articles distributed under the Creative Commons Attribution License, which permits unrestricted use, distribution, and reproduction in any medium, provided the original work is properly cited.

Editorial Board

M. Sabry Abdel-Mottaleb, Egypt
Nihal Ahmad, USA
Nicolas Alonso-Vante, France
Wayne A. Anderson, USA
Vincenzo Augugliaro, Italy
Detlef W. Bahnemann, Germany
Mohammad A. Behnajady, Iran
Ignazio Renato Bellobono, Italy
Raghu N. Bhattacharya, USA
Gion Calzaferri, Switzerland
Adriana G. Casas, Argentina
Wonyong Choi, Republic of Korea
Věra Cimrova, Czech Republic
Vikram L. Dalal, USA
D. Demetriou Dionysiou, USA
Mahmoud M. El-Nahass, Egypt
Ahmed Ennaoui, Germany
Chris Ferekides, USA
David Ginley, USA
Beverley Glass, Australia
Shinya Higashimoto, Japan
Chun-Sheng Jiang, USA
Yadong Jiang, China

Shahed Khan, USA
Cooper H. Langford, Canada
Yuexiang Li, China
Stefan Lis, Poland
Niyaz Mohammad Mahmoodi, Iran
Dionissios Mantzavinos, Greece
Ugo Mazzucato, Italy
Jacek Miller, Poland
Kazuhiko Mizuno, Japan
Jarugu N. Moorthy, India
Franca Morazzoni, Italy
Fabrice Morlet-Savary, France
Ebinazar B. Namdas, Australia
Maria da Graça P. Neves, Portugal
Leonidas Palilis, Greece
Leonardo Palmisano, Italy
Ravindra K. Pandey, USA
David Lee Phillips, Hong Kong
Pierre Pichat, France
Xie Quan, China
Tijana Rajh, USA
Peter Robertson, UK
Avigdor Scherz, Israel

Lukas Schmidt-Mende, Germany
Panagiotis Smirniotis, USA
Zofia Stasicka, Poland
Juliusz Sworakowski, Poland
Nobuyuki Tamaoki, Japan
Gopal N. Tiwari, India
Nikolai V. Tkachenko, Finland
Veronica Vaida, USA
Roel van De Krol, Germany
Mark van Der Auweraer, Belgium
Ezequiel Wolcan, Argentina
Man Shing Wong, Hong Kong
David Worrall, UK
Fahrettin Yakuphanoglu, Turkey
Minjoong Yoon, Republic of Korea
Jimmy C. Yu, Hong Kong
Hongtao Yu, USA
Jun-Ho Yum, Switzerland
Klaas Zachariasse, Germany
Lizhi Zhang, China
Jincai Zhao, China

Contents

Prompt and Delayed Fluorescences, Korkut Yegin, Ş. İpek Karaaslan, Necdet Aslan
Volume 2012, Article ID 786384, 2 pages

Structural Configuration of Myelin Figures Using Fluorescence Microscopy, Lobat Tayebi, Masoud Mozafari, Daryoosh Vashae, and Atul N. Parikh
Volume 2012, Article ID 685617, 7 pages

Absorption and Fluorescence Spectroscopy of 1,2 : 3,4-Dibenzanthracene, Fuat Bayrakceken, Korkut Yegin, Erdal Korkmaz, Yakup Bakis, and Bayram Unal
Volume 2012, Article ID 563090, 4 pages

Resonance Fluorescence of Fused Silica by the Depopulation of the Ground State, Fuat Bayrakceken and Korkut Yegin
Volume 2012, Article ID 359384, 3 pages

Thin Films Prepared from Nanometer Size TiO_2 Absorbs Millimeter Waves, Mehmet Ali Yesil, Korkut Yegin, Mustafa Culha, and Esen Efeoglu
Volume 2012, Article ID 494636, 5 pages

Fluorescence, Decay Time, and Structural Change of Laser Dye Cresyl Violet in Solution due to Microwave Irradiation at GSM 900/1800 Mobile Phone Frequencies, Fuat Bayrakceken and Korkut Yegin
Volume 2012, Article ID 965426, 4 pages

Optical Energy Transfer Mechanisms: From Naphthalene to Biacetyl in Liquids and from Pyrazine to Biacetyl, Fuat Bayrakceken, Korkut Yegin, Erdal Korkmaz, Yakup Bakis, and Bayram Unal
Volume 2012, Article ID 239027, 4 pages

Evaluation of Acoustic Cavitation in Terephthalic Acid Solutions Containing Gold Nanoparticles by the Spectrofluorometry Method, Ameneh Sazgarnia and Ahmad Shanei
Volume 2012, Article ID 376047, 5 pages

Detection of Ammonia in Liquids Using Millimeter Wave Spectroscopy, Hilmi Ozturk, Hakki Nazli, Korkut Yegin, and Mehmet Sezgin
Volume 2012, Article ID 362084, 4 pages

Editorial

Prompt and Delayed Fluorescences

Korkut Yegin,¹ Ş. İpek Karaaslan,² and Necdet Aslan²

¹Department of Electrical and Electronics Engineering, Yeditepe University, 34755 Istanbul, Turkey

²Physics Department, Yeditepe University, 34755 Istanbul, Turkey

Correspondence should be addressed to Korkut Yegin, kyegin@yeditepe.edu.tr

Received 6 December 2012; Accepted 6 December 2012

Copyright © 2012 Korkut Yegin et al. This is an open access article distributed under the Creative Commons Attribution License, which permits unrestricted use, distribution, and reproduction in any medium, provided the original work is properly cited.

The photophysical and chemical behaviors of certain materials manifest themselves in the form of prompt and delayed fluorescence. This issue compiles eight exciting manuscripts on prompt and delayed fluorescence with broad range of applications.

Acoustic cavitation of gold nanoparticles in acid solutions by spectrofluorometry method was explored in detail by A. Sezegania et al. They show that Acoustic cavitation in the presence of gold nanoparticles provides a new way for improving therapeutic effects on the tumors in sonodynamic therapy.

Structural configuration of myelin figures using fluorescence microscopy was shown in this special issue by L. Tayebi et al. Employing epifluorescent microscopy, they studied the lifetime and configuration of myelin figures in experiment of lipid hydration. They found direct correlations between the lifetime of myelin figures and the experimental conditions such as temperature, density of the parent stack, and the hydrophobicity of the substrate.

Microwave irradiation effects on the electronic structure of cresyl violet in solution was studied by F. Bayrakceken et al. These changes are important because Cresyl violet is often used as a staining agent for studying changes on DNA and RNA-rich compounds in tissues. Based on absorption spectra, they concluded that cresyl violet molecular structure due to the microwave irradiation was changed and the phononic product could not be used as a laser-dye after microwave irradiation.

In another study by F. Bayrakceken et al. discrete absorption and resonance coherent fluorescence line of silicon dioxide were recorded photographically and discrete fluorescence was observed at room temperature using high photon flux excitation spectroscopy. They state that it is possible

to use fused silica as a laser material in the UV or as a UV detector with its inherit visible-blind property.

H. Ozturk and his colleagues showed that the inversion of ammonia molecule which results in split rotational spectral lines can be used to detect presence of ammonia in water for counter bioterrorism applications. Millimeter wave absorption using a coherent source and detector was used to provide experimental evidence.

F. Bayrakceken et al. analyzed polycyclic aromatic hydrocarbon compound, 1,2:3,4-dibenzanthracene spectroscopically in ethanol. Ultraviolet absorption spectra and fluorescence measurements were performed to show that Stokes' lines were discernible. Being a carcinogenic compound, the detection of 1,2:3,4-dibenzanthracene presence in environment as a pollutant is crucial in many applications.

M. A. Yesil studied millimeter wave absorption of TiO₂ nanoparticles deposited on glass assembly. Absorption of millimeter waves by a thin film of TiO₂ nanoparticles at distinctive frequency band was shown with a network analyzer.

Optical energy transfer at room temperature plays an important role in many applications. Electronically excited naphthalene with 200–260 nm ultraviolet (UV) light emits photons in its emission band and the emitted photons are absorbed by biacetyl, and then, excited biacetyl phosphorescence. The resulting phosphorescence was shown to be very stable with emission peak at 545 nm for different excitation wavelengths from 200 to 260 nm. Similar optical energy transfer was shown from pyrazine to biacetyl. Optical energy transfer mechanisms were detailed.

By compiling this special issue, we hope to enrich our readers and researchers understanding and broad applications of prompt and delayed fluorescence.

Acknowledgment

We also pay special tribute to Professor Fuat Bayrakceken, an inspirational scientist, whom we lost unexpectedly during the preparation of this special issue. Professor Bayrakceken was mostly known with his discovery of a new fluorescence type known as B-type fluorescence.

*Korkut Yegin
Ş. İpek Karaaslan
Necdet Aslan*

Research Article

Structural Configuration of Myelin Figures Using Fluorescence Microscopy

Lobat Tayebi,¹ Masoud Mozafari,¹ Daryoosh Vashaee,² and Atul N. Parikh³

¹ Helmerich Advanced Technology Research Center, School of Material Science and Engineering, Oklahoma State University, Tulsa, OK 74106, USA

² Helmerich Advanced Technology Research Center, School of Electrical and Computer Engineering, Oklahoma State University, Tulsa, OK 74106, USA

³ Department of Chemical Engineering and Material Science and Department of Biomedical Engineering, University of California, Davis, CA 95616, USA

Correspondence should be addressed to Lobat Tayebi, lobat.tayebi@okstate.edu and Atul N. Parikh, anparikh@ucdavis.edu

Received 5 May 2012; Accepted 18 October 2012

Academic Editor: Korkut Yegin

Copyright © 2012 Lobat Tayebi et al. This is an open access article distributed under the Creative Commons Attribution License, which permits unrestricted use, distribution, and reproduction in any medium, provided the original work is properly cited.

Using epifluorescence microscopy, the configuration of myelin figures that are formed upon hydration of lipid stack was studied qualitatively. Little knowledge is currently available for conditions that determine the diameter of myelin figures and their degree of multilamellarity. Examining more than 300 samples, we realized that there are distinct populations of myelin figures protruding from discrete regions of lipid stack. Each population contains myelin figures with similar diameters. This indicates a direct relationship between local characteristics of parent lipid stack and the diameter of myelin figures. Evidenced by fluorescent images, we classified all the observed myelin figures into three major groups of (1) solid tubes, (2) thin tethers, and (3) hollow tubes. Solid tubes are the most common structure of myelin figures which appeared as dense shiny cylinders. Thin tethers, with long hair-shaped structure, were observed protruding from part of lipid plaque which is likely to be under tension. Hollow tubes were protruded from the parts that are unpinned from the substrate and possibly under low or no tension. The abrupt change in the configuration of myelin figures from solid tubes to hollow ones was described in a reproducible experiment where the pinned region of the parent stack became unpinned. Our observations can indicate a relation between the membrane tension of the source material and the diameter of the myelin figures.

1. Introduction

Concentrated mesophases of membrane-forming lipids in water deform readily producing multilamellar cylindrical tubules in the presence of external forces via a close interplay of fluidity and elasticity [1, 2]. Similar multilamellar tubes, also known as myelin figures, are typically originating from and connected to reservoir of dense lipid plaques [3].

Such multilamellar myelin figures which consist of many different diameters [4] can be found in various types of biological organelles and cells in their normal or diseased shapes [5]. Although they can be established as transient structures too, many of them are long lived with very slow dynamics, which can be assumed as quasi-equilibrium structures such

as the myelin figures in aged red blood cell [6], kidney [7], and lung [8, 9]. A prominent example is the existence of myelin figure in pulmonary lining, an extracellular lipid-protein coat at the alveolar surface, which facilitates decrease in surface tension when lungs deflate [10].

A common property of many of these living myelin structures is that they are stable protrusions from concentrated lipid plaques in body [3, 11].

Other than different phospholipids which are an important source for myelin figure formation [2, 12, 13], ionic surfactants including Aerosol OT (AOT) [14, 15] and non-ionic surfactants including pentaethylene glycol lauryl ether (C12E5) [16] and triethylene glycol lauryl ether (C12E3) [15, 17] can also produce myelin figures.

Beyond their biological significance, membrane tubules are also important, for instance, in the realization of artificial nanofluidic networks [18, 19].

Myelin figures can protrude from different sources due to different reasons especially in complex biological systems. However, the structure and configuration of all myelin figures is very similar to what is formed via simple hydration of dry lipid stack. Thus, this simple *in vitro* experiment is usually replaced to study the features of myelin figure production [1, 12, 14, 20–23].

Although unilamellar lipid tethers, such as those obtained by exerting local force on giant unilamellar vesicles, have been extensively studied both theoretically and experimentally [24], efforts aimed purportedly on studying the various configuration of myelin figures and how their diameters correlate with the experimental condition are sparse.

In this paper, using fluorescence microscopy, we studied the life time and different structural morphologies of myelin figures in the experiment of hydrating different kinds of dry lipid plaque. The experiments were done employing lipid stacks with various densities at different temperatures on both hydrophobic and hydrophilic substrates. We categorized the observed multilamellar myelin figures into three major groups of (1) solid tubes, (2) thin tethers, and (3) hollow tubes. These three groups were usually protruded in distinct population from separate regions of parent lipid stack. This can be an evidence to show the relation between the local characteristic of parent lipid stack and the myelin figure configuration. However, in a systematic set of experiments, we could not find a direct correlation between the diameter of myelin figures and the thickness of parent lipid stack.

2. Material and Method

1,2-dimyristoyl-*sn*-glycero-3-phosphocholine (DMPC), 1-palmitoyl-2-oleoyl-*sn*-glycero-3-phosphocholine (POPC) and 1,2-dioleoyl-*sn*-glycero-3-phosphocholine were purchased from Avanti Polar Lipids. Texas Red DHPE and fluorescein sodium salt were purchased from Invitrogen and Sigma Aldrich, respectively.

The solutions of lipid and chloroform were prepared at different concentrations (0.5 mg/mL–250 mg/mL). 1 mol% of Texas Red DHPE was added to the solution as a fluorescence marker.

0.5–1 μ L of the lipid/chloroform solution was dropped on a substrate. The drops were air-dried for 10 minutes at room condition and were placed in vacuum for 12 hours for complete evaporation of chloroform. After this procedure, the lipid plaque (dry drop) was completely pinned to the substrate. 3–5 mL of DI water was added to a small Petri dish containing the dry lipid drop on a substrate. The water covers the total area of the substrate. Myelin figures start growing from the edge of the lipid drop right after hydration above the phase transition temperature (T_m) of the lipid.

The experiments were done with various kinds of lipids including DMPC, POPC, and DOPC and were examined

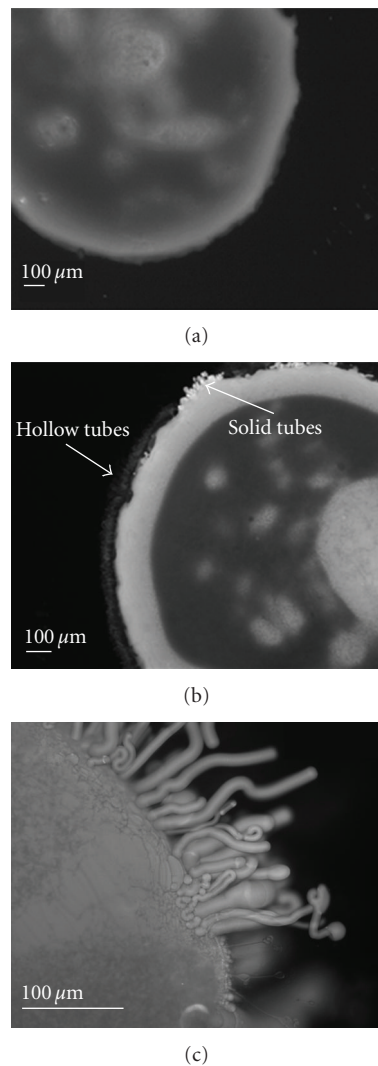


FIGURE 1: Fluorescent images of (a) dry lipid plaque (b) after myelin figure formation upon hydration. As can be seen different groups of myelin figures are protruding from distinct regions (c) higher magnification of solid tubes.

on both hydrophobic and hydrophilic substrates. Freshly piranha-etched clean glass slides were employed as a hydrophilic substrate. As hydrophobic substrates, we used silane-coated glass slides.

3. Result and Discussions

The dry lipid plaque and the myelin figures that are formed after hydration of the plaque were imaged using an inverted epifluorescence microscope (Nikon, Melville, NY). The typical form of a dry lipid plaque before hydration and the drop decorated by myelin figures after hydration are shown in Figures 1(a) and 1(b).

The lifetime of myelin figures was affected by the condition of the experiment. It was longer in the experiments using hydrophobic substrate than in the ones using a hydrophilic substrate. Also experiments with different initial

concentrations of lipid/chloroform solution indicated that higher concentrations make more stable myelin figures. Both of the above conditions (quality of the substrate and the initial concentration of lipid solution) had direct influence on the configuration of dry lipid plaque. The dry drops on the hydrophobic substrate were circular in shape with well-defined dense edge. However, on the hydrophilic substrate most of the drops had a crooked shape with uneven and thin edge. Configuration of the dry drop also depended on the initial concentration of lipid/chloroform solution. The higher the concentration of the solution is, the denser and the thicker is the resulting dry lipid plaque. Since the material source of the myelin figures was the local stack of lipid they were protruding from, myelin figures were more stable when the parent lipid plaque was denser.

Also, the lifetime of myelin figures was related to the temperature. The experiments were done at different temperatures ranging from 2°C to 40°C. The hydrating water was also kept at the set temperature. Myelin figures are more stable at low temperature most likely due to the slower dynamics.

Based on our experimental result, the lifetime of myelin figures can be varied from less than a minute to about 15 hours. For example, myelin figures at 2°C protruded from a dense lipid plaque dried from a solution of lipid/chloroform at 250 mg/mL on hydrophobic substrate could be easily stable more than 13 hours. On the contrary, hydration of dry lipid plaque from initial solution concentration of 0.5 mg/mL on hydrophilic substrate at 40°C could not make myelin figures with lifetime more than a minute. We concluded that the lower temperature, higher concentration (denser parent lipid plaque), and hydrophobicity of the substrate increase the stability of myelin figures.

Although there are correlations between the lifetime of myelin figures and the experimental condition, we hardly could find any relation between the diameter of the tubular structure of myelin figures and the conditions of experiments such as temperature and concentration of initial solution.

The exact reason for having myelin figures in different tubular diameters is not clearly understood yet and has been an open question for many years [1, 17]. In a recent study [1], it was suggested that the diameter of a myelin figure is directly comparable to the thickness of the parent lipid plaque from which they emerged. Their conclusion is based on the confocal images of junction between the parent lipid stack and the myelin figures under a fixed set of conditions. However, in a series of experiments that we have done with parent lipid stacks of variable thickness ranging from 7 μm to 25 μm , little correlation was found between the thickness of the parent stack and the diameter of myelin figures that protruded from them. Figure 2 shows examples of myelin figures protruded from lipid stack with average thicknesses of 13, 17, and 24 μm . As can be seen in this figure, the diameter of majority of myelin figures protruded from 17 μm thick lipid plaque is larger than the ones protruded from two other lipid plaques.

Examining more than 300 samples, we realized that a myelin figure does not randomly adopt a diameter. We found groups of myelin figures with similar diameter and structure

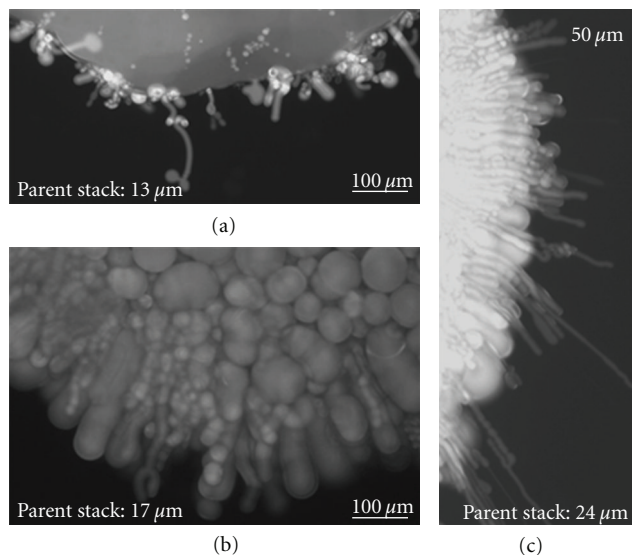


FIGURE 2: Comparison of average diameter of myelin figures protruded from parent lipid plaques with different thicknesses shows no exact correlation between the thicknesses of parent stack and the diameter of myelin figures.

are growing from separate regions of the parent plaque. All the observed myelin figures can be categorized in three groups: (1) solid tubes, (2) thin tethers, and (3) hollow tubes. Examples of these groups are shown in Figure 3.

As we discussed earlier, myelin figures have the morphology of multilamellar cylindrical tubes. The three observed configurations of solid tubes, thin tethers, and hollow tubes were defined based on two structural terms of multilamellar tubes: (1) core radius and (2) number of lamellae.

Solid tubes represent tubular structures with large number of lamellae. As can be seen in Figure 3(a), in solid tubes, the total diameter of the tube is considerably larger than the diameter of its core. Using fluorescence microscopy, we observed this group of myelin figures as fat shiny tubes with high fluorescence intensity. Figure 3(a) represents the examples of fluorescent image of solid tubes.

Thin tethers were defined as a group of myelin figures with low number of lamellae and small core radius. The total diameter of thin tethers can be comparable to the diameter of the core. In fluorescent images, they appeared as shiny thin hair-shaped tubes (Figure 3(b)).

Myelin figures in the last group, hollow tubes, are the ones with low number of lamellae and large core radius. The total thickness of the layers in a hollow tube can be less than the diameter of the core. In fluorescence microscopy, hollow tubes were observed as tubes with very low intensity (Figure 3(c)). These three groups usually could be found in distinct and separated populations in different regions of the parent lipid plaques instead of having mixed population of them from one region. For example, Figure 1(b) represents an example of this fact where solid tubes and hollow ones are formed from different regions of lipid plaque.

The exact origin of the different configuration in different myelin figure groups is not clearly understood. However,

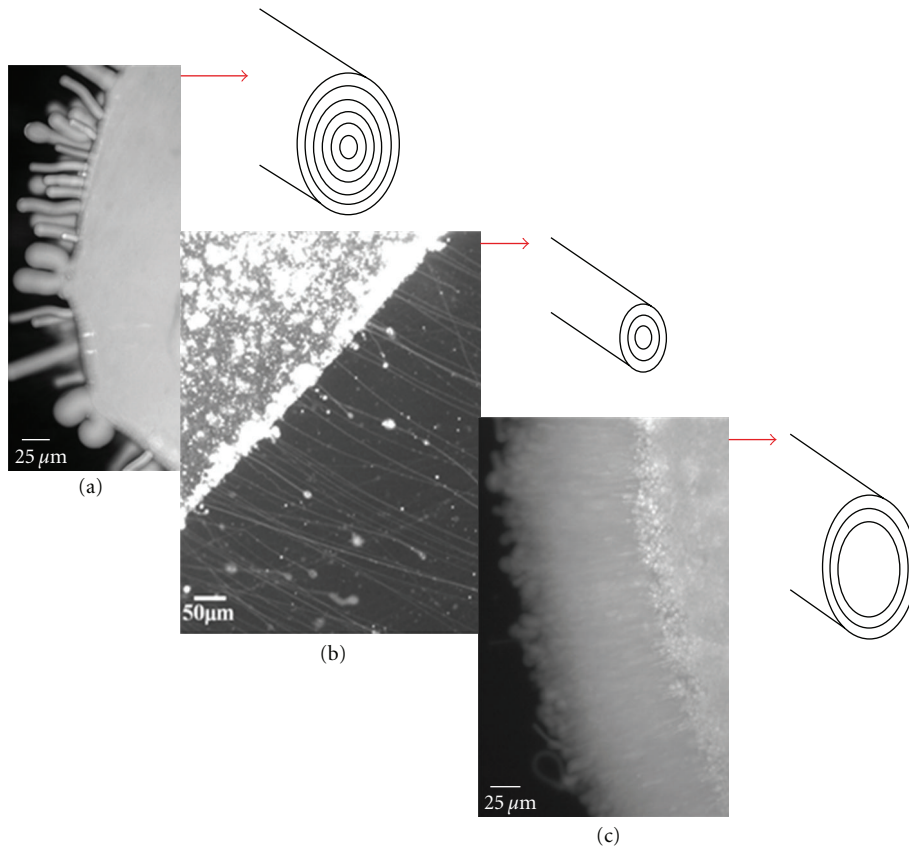


FIGURE 3: Wide-area fluorescent micrographs illustrating three major types of tubule morphologies observed upon the hydration of dry stack lipid doped with 1 mol% Texas Red by water above their phase transition temperature. (a) Solid tubes: large number of lamellar. (b) Thin tethers: low number of lamellae with small core radius. (c) Hollow tubes: low number of lamellae with large core radius.

we suspect that there is a direct relation between the local characteristic of the parent lipid plaque and morphology of the myelin figures. Solid tubes are normal and the most common structure of myelin figures. We observed that the thin tethers can be protruded from the area that the lipid plaque had less wrinkling in the surface. Apparently, wrinkling (as reservoir of lipid) decreases the membrane tension. On the other hand, hollow tubes are constantly observed to be grown from the regions of lipid plaques that are unpinned from the substrate and can have lower membrane tension than normal. Figure 4 shows an example of this fact for a hollow tube in a very reproducible experiment described below. A dry DMPC plaque, which was pinned to the substrate, was immersed under water for couple of minutes at temperature below the phase transition of DMPC ($T_m \approx 24^\circ\text{C}$). Note that myelin figures cannot be formed below T_m . This causes some parts of the edge of the drop to be unpinned from the substrate but still attached to the whole drop. Now we have two distinct regions of lipid: pinned and unpinned. The temperature increased very slowly to the above phase transition temperature, where the myelin figures can be formed. Interestingly, always, two very distinct populations of myelin figures were observed, hollow and solid tubes (e.g., see Figure 4(a1)). Hollow tubes protrude from the unpinned region and Solid tubes from

the pinned region of lipid plaque. By the time, when other parts of the plaque become unpinned, the solid tubes are replaced by hollow tubes. Snapshots of this process are shown in Figure 4, (a1)–(a3). To further validate this hypothesis, we did the similar experiment by letting the whole lipid plaque to be unpinned and suspended from the substrate at temperature lower than T_m . In this case, when we increase the temperature to above T_m , only one population of myelin figures grows (Figure 4(b)).

To discriminate between the hollow and solid morphologies of myelin tubes, we relied on the fluorescent emission from the trace concentrations of lipid soluble dyes embedded within the lipid phase. The dramatic differences in the fluorescence intensities from the well-focused images of populations of myelin figures observed in single samples within single wide-field fluorescent micrographs ($500\ \mu\text{m} \times 400\ \mu\text{m}$) can stem from a variety of sources. While small variations (within 5–10%) can result from subtle differences in lipid microenvironment, the large variations we observed indicate substantial differences in fluorophore populations. Furthermore, the lipid-conjugated fluorophores used were not sensitive to lipid packing or phase state, thus, allowing us to conclude that their intensity difference does not reflect their preferential accumulation or partitioning into one morphology (e.g., solid versus hollow)

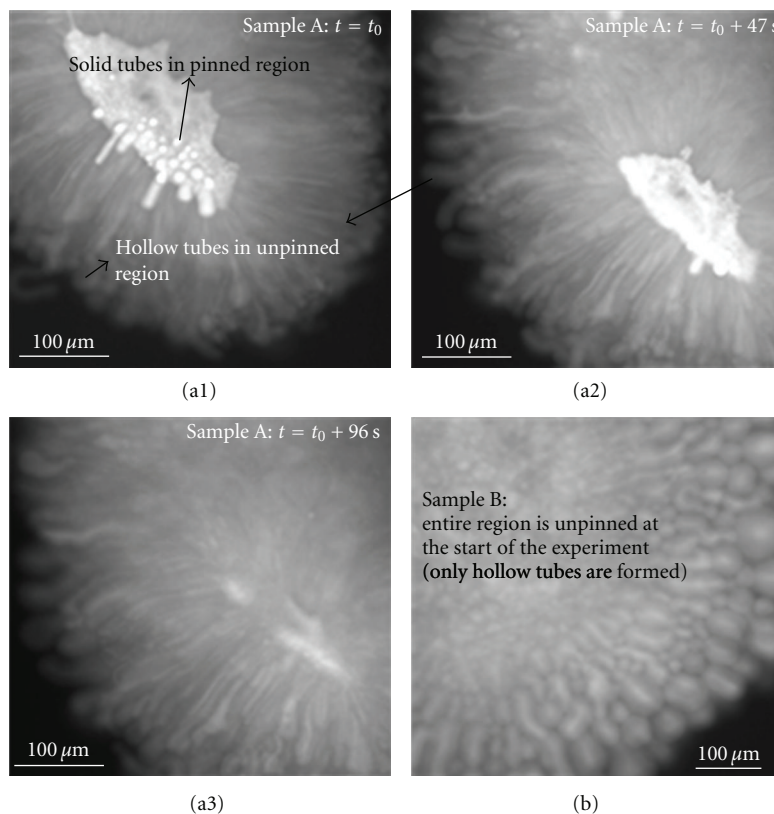


FIGURE 4: (a1)–(a3) Epifluorescence micrographs reveal coexistence of solid and hollow tubes emanating from single plaque of DMPC (sample A) while edge of the plaque is unpinned from the substrate and its central part is pinned. Protrusion is formed when initially dry lipid plaque is hydrated below T_m and then heated to above its T_m value. Solid tubes appear from the pinned region and hollow tubes protrude from the unpinned region (a1) and (a2). Over time, the entire plaque becomes unpinned, and all solid tubes retract and are replaced by hollow tubes (a3). (b) Fully suspended DMPC plaques in water produce exclusively hollow tubes. (DMPC is doped with 0.75 mol% TR.)

over the other. Based on these considerations, we assumed direct proportionality between fluorescence intensity and the average lipid density. Following this criterion, myelin figures with faint fluorescence (in well-focused image) can be conveniently categorized as “hollow” tubes whereas ones with strong fluorescence (fourfold above the hollow ones) can be assigned to the “solid” tube. (Note that to have clear images of hollow or solid tubes at a same spot, we usually need to change the focus).

Hollow tubes can be best visualized by differentially staining the lipid and the aqueous phase. To illustrate characterization of hollow tubes, below we performed a dual probe experiment. Here, a plaque of dry POPC, doped with 1 mol% TR-DHPE, was hydrated using 5 mL solution of fluorescently doped water (5×10^{-4} mg/mL Fluorescein/water). The plaque was pinned to the underlying substrate. After formation of myelin figures, the fluorescein-doped water in the aqueous phase was gradually replenished by undoped DI water (by replacing 1 mL solution by DI water in multiple (5–10) iterations). Figure 5 displays a two-color fluorescent image (a) as well as single color images (b) and (c). The images were obtained when part of the parent plaque had unpinned from the substrate, thus, providing condition for the formation of hollow tubes. Unfocused

hollow myelin figures often appeared as faint and blurry features surrounding the parent plaque. However, well-focused ones (such as seen in Figure 5) revealed distinct fluorescence from both the lipid and the aqueous phase, consistent with the core-shell structure of hollow myelin figures discussed in Figure 3(c).

4. Conclusion

Employing epifluorescence microscopy, we studied the lifetime and configuration of myelin figures in experiment of lipid hydration. There were direct correlations between the lifetime of myelin figures and the experimental conditions such as temperature and density of the parent stack and the hydrophobicity of the substrate. Denser parent stack on hydrophobic substrate at low temperature can produce more stable myelin figures with greater lifetime (more than 13 hours). There was evidence that indicated the diameter of myelin figures was related to the local characteristics of the parent stack. However, such characteristics were not easily quantifiable in the experiments. Specifically, we observed that distinct populations of myelin figures with similar configuration protrude from distinct regions of parent stack. Evidenced by fluorescent images, we classified

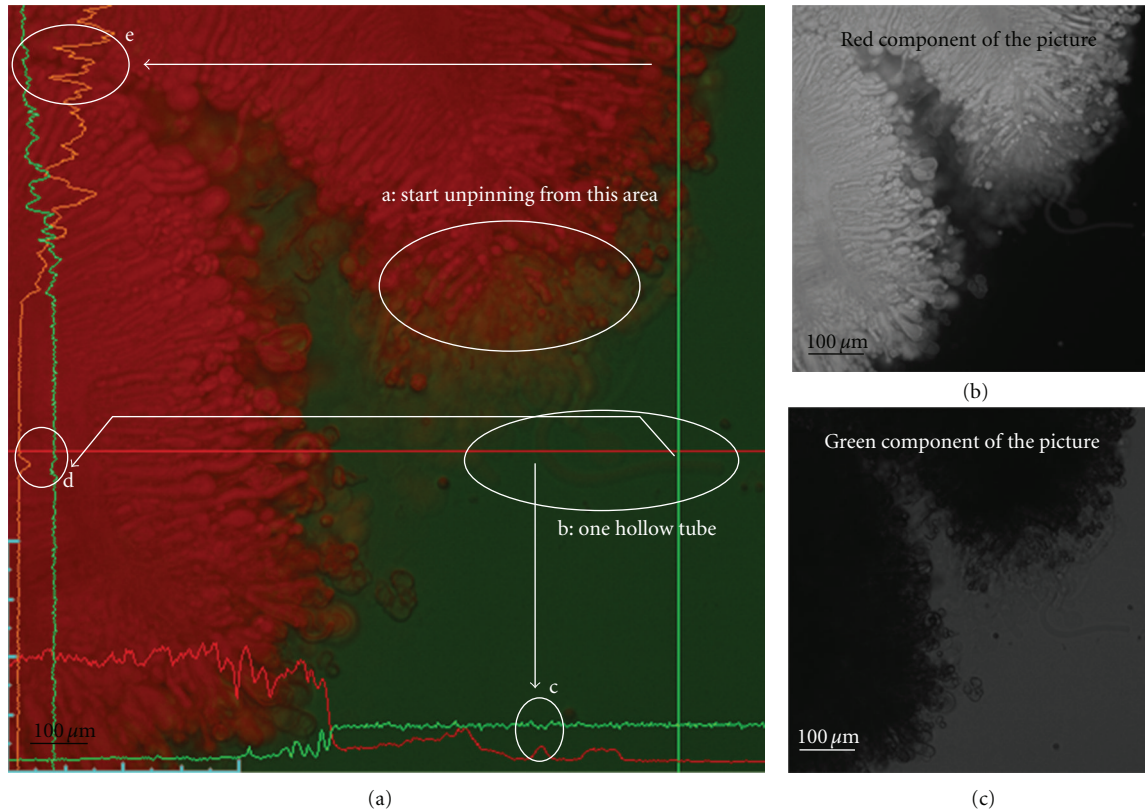


FIGURE 5: POPC, 1 mol% TR-DHPE, room temperature, hydrate solution of fluorescein/DI water 5×10^{-4} mg/mL Fluorescein. (a) Shows the two-color image; (b) and (c) are the same image with only one-color component (red (lipid) or green (water)). Region a: in (a) shows the area where the plaque of lipid start unpinning from the substrate. So, the myelin figures growing from that area have a hollow shape. Region b: shows one of these hollow tubes. (Circles c and d) refer to the intensity of two areas in the hollow tube which can be compared with the environment of a solid tube (Circle e).

all the observed myelin figures in three major groups of (1) solid tubes, (2) thin tethers, and (3) hollow tubes which were analyzed in this paper. We defined first group as multilamellar tubes with a large number of lamellae in which the total thickness of multilamellar layer is much thicker than the core radius. The second and third groups consist of myelin figures with a low number of lamellae. In the second group, the total thickness of layers is comparable to the core diameter. However, in the third group, the core diameter is very large compared to the total thickness of layers in a way that the myelin figures look like hollow tubes. Solid tubes are the most common structure of myelin figures. On the basis of our observation, thin tethers are more prone to be formed from the source lipid with higher membrane tension. On the other hand, our experiments showed that hollow tubes are mostly formed when part of the parent lipid plaque is unpinned from substrate so its tension was decreased. In this occasion, an abrupt change from solid tube to hollow ones can be observable reproducibly.

References

- [1] L. N. Zou and S. R. Nagel, "Stability and growth of single myelin figures," *Physical Review Letters*, vol. 96, no. 13, Article ID 138301, pp. 1–4, 2006.
- [2] W. Harbich and W. Helfrich, "The swelling of egg lecithin in water," *Chemistry and Physics of Lipids*, vol. 36, no. 1, pp. 39–63, 1984.
- [3] W. Stoeckenius, "OsO₄-Fixierung intrazellulärer myelinfiguren," *Experimental Cell Research*, vol. 13, no. 2, pp. 410–414, 1957.
- [4] S. C. Watkins and R. D. Salter, "Functional connectivity between immune cells mediated by tunneling nanotubules," *Immunity*, vol. 23, no. 3, pp. 309–318, 2005.
- [5] D. G. Dervichian, "Swelling and molecular organisation in colloidal electrolytes," *Transactions of the Faraday Society*, vol. 42, pp. B180–B187, 1946.
- [6] M. Besisi, *Living Blood Cells and Their Ultrastructure*, Springer, Berlin, Germany, 1973.
- [7] N. Basic-Jukic, M. Coric, P. Kes, L. J. Bubic-Filipi, J. Pasini, and I. Mokos, "Anderson-Fabry disease in kidneys from deceased donor," *American Journal of Transplantation*, vol. 7, no. 12, pp. 2829–2833, 2007.
- [8] F. R. Poulain, L. Allen, M. C. Williams, R. L. Hamilton, and S. Hawgood, "Effects of surfactant apolipoproteins on liposome structure: implications for tubular myelin formation," *American Journal of Physiology*, vol. 262, no. 6, pp. L730–L739, 1992.
- [9] H. Fehrenbach, S. Tews, A. Fehrenbach et al., "Improved lung preservation relates to an increase in tubular myelin-associated surfactant protein A," *Respiratory Research*, vol. 6, article 60, 2005.

- [10] R. J. Sanderson and A. E. Vatter, "A mode of formation of tubular myelin from lamellar bodies in the lung," *Journal of Cell Biology*, vol. 74, no. 3, pp. 1027–1031, 1977.
- [11] A. Policard, A. Collet, and S. Pregermain, "Electron microscopic study of the first stages of lipophanerosis in histiocytes," *Comptes Rendus Hebdomadaires Des Seances De L Academie Des Sciences*, vol. 246, no. 25, pp. 3405–3406, 1958.
- [12] J. R. Huang, L. N. Zou, and T. A. Witten, "Confined multilamellae prefer cylindrical morphology: AAAA theory of myelin formation," *European Physical Journal E*, vol. 18, no. 3, pp. 279–285, 2005.
- [13] I. Sakurai, T. Suzuki, and S. Sakurai, "Cross-sectional view of myelin figures," *Biochimica Et Biophysica Acta*, vol. 985, no. 1, pp. 101–105, 1989.
- [14] M. Buchanan, J. Arrault, and M. E. Cates, "Swelling and dissolution of lamellar phases: role of bilayer organization," *Langmuir*, vol. 14, no. 26, pp. 7371–7377, 1998.
- [15] A. P. Kennedy, J. Sutcliffe, and J. X. Cheng, "Molecular composition and orientation in myelin figures characterized by coherent anti-stokes Raman scattering microscopy," *Langmuir*, vol. 21, no. 14, pp. 6478–6486, 2005.
- [16] W. J. Benton, K. H. Raney, and C. A. Miller, "Enhanced videomicroscopy of phase transitions and diffusional phenomena in oil-water-nonionic surfactant systems," *Journal of Colloid And Interface Science*, vol. 110, no. 2, pp. 363–388, 1986.
- [17] L. Reissig, D. J. Fairhurst, J. Leng, M. E. Cates, A. R. Mount, and S. U. Egelhaaf, "Three-dimensional structure and growth of myelins," *Langmuir*, vol. 26, no. 19, pp. 15192–15199, 2010.
- [18] E. Evans, H. Bowman, A. Leung, D. Needham, and D. Tirrell, "Biomembrane templates for nanoscale conduits and networks," *Science*, vol. 273, no. 5277, pp. 933–935, 1996.
- [19] T. Roopa, N. Kumar, S. Bhattacharya, and G. V. Shivashankar, "Dynamics of membrane nanotubulation and DNA self-assembly," *Biophysical Journal*, vol. 87, no. 2, pp. 974–979, 2004.
- [20] L. N. Zou, "Myelin figures: the buckling and flow of wet soap," *Physical Review E*, vol. 79, no. 6, Article ID 061502, 2009.
- [21] C. D. Santangelo and P. Pincus, "Coiling instabilities of multilamellar tubes," *Physical Review E*, vol. 66, no. 6, Article ID 061501, 2002.
- [22] K. C. Lin, R. M. Weis, and H. M. McConnell, "Induction of helical liposomes by Ca^{2+} -mediated intermembrane binding," *Nature*, vol. 296, no. 5853, pp. 164–165, 1982.
- [23] V. Frette, I. Tsafirir, M. A. Guedeau-Boudeville, L. Jullien, D. Kandel, and J. Stavans, "Coiling of cylindrical membrane stacks with anchored polymers," *Physical Review Letters*, vol. 83, no. 12, pp. 2465–2468, 1999.
- [24] I. Derényi, F. Jülicher, and J. Prost, "Formation and interaction of membrane tubes," *Physical Review Letters*, vol. 88, no. 23, pp. 2381011–2381014, 2002.

Research Article

Absorption and Fluorescence Spectroscopy of 1,2:3,4-Dibenzanthracene

Fuat Bayrakceken,¹ Korkut Yegin,² Erdal Korkmaz,³ Yakup Bakis,³ and Bayram Unal³

¹ Department of Biomedical Engineering, Yeditepe University, 34755 Istanbul, Turkey

² Department of Electrical and Electronics Engineering, Yeditepe University, 34755 Istanbul, Turkey

³ Bionanotechnology Research Center, Fatih University, 34500 Istanbul, Turkey

Correspondence should be addressed to Yakup Bakis, ybakis@fatih.edu.tr

Received 18 July 2012; Accepted 19 October 2012

Academic Editor: Ipek Karaaslan

Copyright © 2012 Fuat Bayrakceken et al. This is an open access article distributed under the Creative Commons Attribution License, which permits unrestricted use, distribution, and reproduction in any medium, provided the original work is properly cited.

Polycyclic aromatic hydrocarbon compound, 1,2:3,4-dibenzanthracene, is spectroscopically analyzed in ethanol. Ultraviolet absorption spectra were taken and fluorescence measurements were performed. From absorption and emission spectra, Stokes' lines were clearly discernible and these shifts were recorded. Being a carcinogenic compound, the detection of 1,2:3,4-dibenzanthracene presence in the environment as a pollutant with adverse genotoxic effects is vital.

1. Introduction

Absorption and emission spectroscopy of dibenzanthracene (DBA) isomers such as 1,2,5,6-DBA, 1,2,7,8-DBA have been analyzed in polymer matrices [1, 2]. Amorphous solids such as polymethylmethacrylate remain relatively rigid even at high temperatures and DBA molecules cannot move freely in such solids, thus making them ideal for time resolved absorption and fluorescence spectra studies of DBA isomers. Singlet and triplet electronic absorption and prompt fluorescence can be readily observed. However, DBA in solvents such as ethanol is much more complicated for absorption and fluorescence spectroscopy. We aim to fill this gap by taking ultraviolet (UV) absorption spectroscopy, fluorescence emission spectroscopy, and Fourier Transform infra-red spectroscopy of 1,2:3,4-dibenzanthracene in ethanol. We also show Stokes' shifts in the fluorescence spectroscopy by measuring the quantum efficiency of the 1,2:3,4-dibenzanthracene and ethanol solution. The molecular structure of 1,2:3,4-dibenzanthracene is shown in Figure 1.

Absorption of light by the molecule excites the molecule to one of the upper electronic singlet states from ground state. Most of the molecules reside in the lowest vibrational state at room temperature and absorption of light initiates upward transitions from this level to higher levels. When the

molecule reaches the first excited singlet state, the molecule can return to any one of the vibrational levels of the ground state by emitting fluorescence. Part of the excited molecules can also return to ground state following other mechanisms such as through quenching processes, photochemical changes, or conversion to triplet state. Hence, fluorescence efficiency becomes less than one [3–12]. In particular, fluorescence spectroscopy of 1,2:3,4-dibenzanthracene reveals clear Stokes' shifts when the molecule is excited in UV.

2. Materials and Methods

1,2:3,4-dibenzanthracene, was of AccuStandard reagent grade, used as received without any further purification and was mixed with ethanol at atmospheric pressure. The concentration of dibenzanthracene was selected as 2.0×10^{-4} M. Two Princeton Instruments Acton Advanced SP2300 model monochromators were used in all optical measurements. These devices have a 600 g/mm grating and a focal length of 300 mm. The measurement setup is illustrated in Figure 2. A 500 W Xenon bulb was mounted in front of the entrance slit of monochromator 1 to obtain the maximum amplitude and the entrance and exit slits were adjusted at $700 \mu\text{m}$ openings. With the help of a computer controlled software,

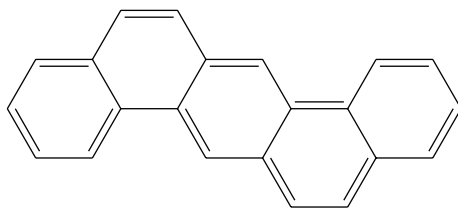


FIGURE 1: 1,2:3,4-dibenzanthracene.

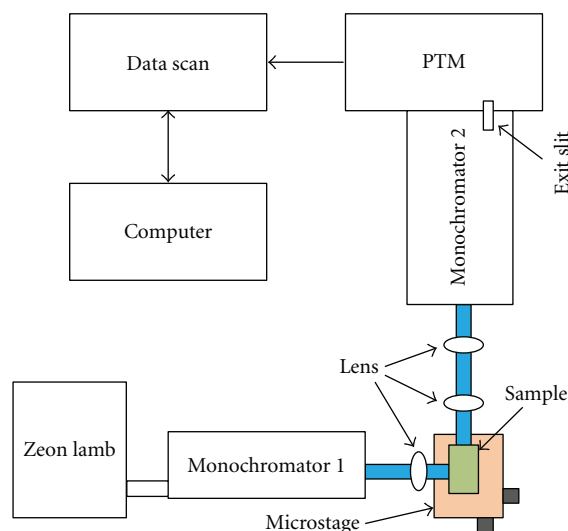


FIGURE 2: Experimental setup block diagram.

monochromatic beams of 300–380 nm wavelength with a 10 nm step were emitted from the exit of monochromator 1. The emitted beam was focused on the sample using a quartz lens to excite the sample. The excited sample was emitting a beam which was perpendicular to the excitation beam. This beam was further focused on the slit of monochromator 2 with the help of sequential lenses where the slit was set again at 700 μm . The alignment was carried out using microstage. The excited beam was scattered from the quartz tube and the liquid interface, however the luminescence originated from the liquid itself. Since the focusing was oriented on the center of the liquid where the luminescence was dense, the excited beam did not arrive at monochromator 2. A computer controlled scan was performed at monochromator 2 between 300 and 550 nm with a step of 1 nm and 500 ms periods. The emitted beam entering through the 700 μm slit from monochromator 2 was converted to electrical signal through the photomultiplier tube (PMT) of the instrument depending on luminescence amplitude. These signals were digitally recorded to a computer through a data scan software. All measurements were performed in a dark room at room temperature and atmospheric pressure. The emitted beam arriving to the PMT was posed with 500 ms time average. Since the Xenon bulb wavelength was filtered at 300–380 nm and the PMT was sensitive to the emission wavelength, a normalization had to be carried out. Because of this, the sample was replaced with a quartz mirror in the measurement setup and the measurement

was repeated. The peaks of the excitation were recorded. The maximum amplitude obtained at 360 nm was used to calculate the normalization coefficient for each wavelength. These coefficients were multiplied with the whole spectrum to perform the required normalization.

The Fourier Transform infrared measurement was carried out with Thermo Scientific and Nicolet FT-IR spectrometer 6700 model. The sample was placed in a quartz tube and placed in the optical path to get a scan starting from 2000 to 11000 cm^{-1} . Before the measurement was started, a background scan was performed and background subtraction was carried out from the sample measurement. All measurements were performed using a computer controlled software with little to no user intervention. The measurements were carried out at room temperature and at atmospheric pressure.

UV spectrophotometer measurements were performed with Thermo Lab Multiskan 1500 model. The liquid mixture, 1,2:3,4-dibenzanthracene in ethanol, and ethanol only solution were measured. Using background subtraction, the spectrum of the mixture was obtained with a computer controlled software. All measurements were performed at room temperature.

3. Results and Discussion

1,2:3,4-dibenzanthracene, a polycyclic aromatic hydrocarbon, has an interesting shape of fluorescence emission

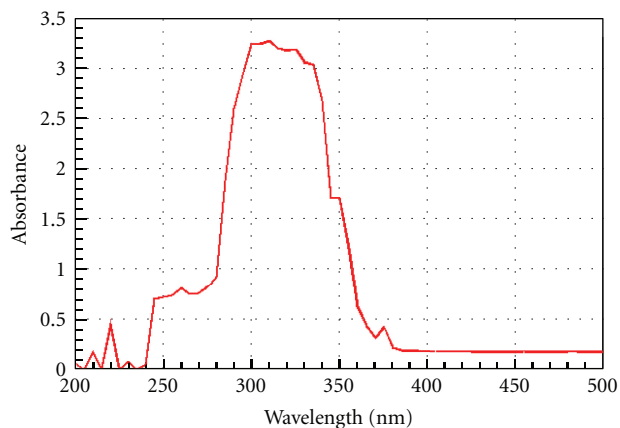


FIGURE 3: UV absorption spectrum.

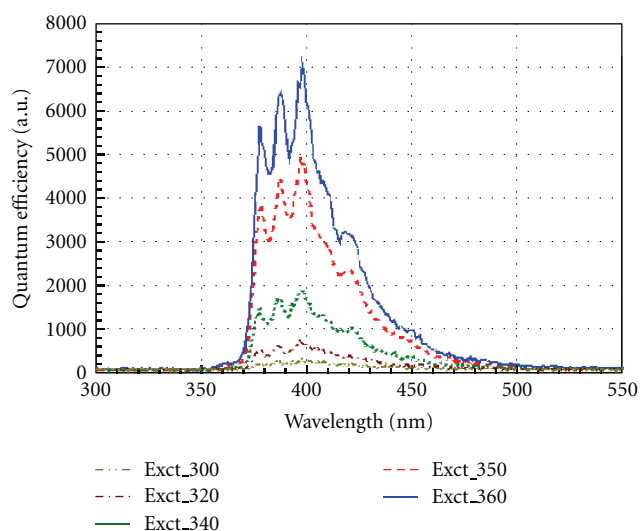


FIGURE 4: Fluorescence spectrum of 1,2:3,4-dibenzanthracene in ethanol.

spectrum because the spectrum is almost an invariant of the wavelength used to excite the molecule. This can be attributed to the fact that the emissions always occur from the S_1 level. The triplet states have lower energies compared to those of corresponding singlet states. The solvent may lead to a breakdown of the spin conservation rule for the molecules, which in turn permit weak $S_0 \rightarrow T_1$ absorption.

The UV absorption spectrum of 1,2:3,4-dibenzanthracene is shown in Figure 3. Although the absorption band is relatively broad, it is strongest around 315 nm. The broad spectrum can be attributed to the onset of π - and σ -bands, strong vibronic coupling, and ionization energies [13, 14].

The fluorescence measurements were carried out as described in Section 2 and the results are displayed in Figure 4. Three sharp peaks, all coincident with the same emission wavelengths are observed. Excitation wavelengths starting from 300 to 360 consistently pointed the same peaks with the highest level at 360 nm of excitation. These are Stokes' shifts of the molecule with relative to the highest absorption wavelength of 315 nm. The absorption and

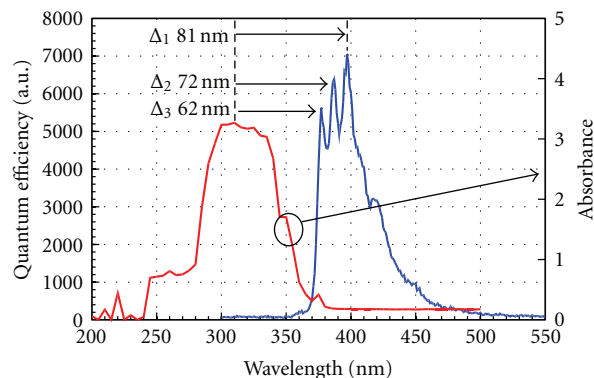


FIGURE 5: Stokes' shifts of 1,2:3,4-dibenzanthracene in ethanol.

emission spectra are shown on the same graph in Figure 5. The three Stokes' shifts were also identified and labeled on the same figure.

4. Conclusions

1,2:3,4-dibenzanthracene is a polycyclic aromatic compound which is carcinogenic and requires careful spectroscopic analysis for monitoring environmental pollutants and genotoxic effects [15–19]. Raman spectroscopy can be a powerful probe for determining chemical composition, but Raman signals can be very weak and easily suppressed by fluorescence (prompt and delayed). Thus, our analysis provides methods in the identification of 1,2:3,4-dibenzanthracene and its isomers.

References

- [1] F. Bayrakçeken, F. Ari, and Z. Telatar, "Spectral image adaptation and visual experience of DBA/PMMA," *Spectrochimica Acta A*, vol. 62, no. 4-5, pp. 1151–1156, 2005.
- [2] F. Bayrakçeken, "Highly sensitive detection of discrete absorption and B-type delayed fluorescence of dibenzanthracene in PMMA," *Spectrochimica Acta A*, vol. 60, no. 13, pp. 3033–3036, 2004.
- [3] S. Rodriguez and H. Offen, "Temperature and pressure dependence of phosphorescence lifetimes in PMMA," *The Journal of Chemical Physics*, vol. 52, no. 2, pp. 586–589, 1970.
- [4] K. A. Hodgkinson and I. H. Munro, "The transient absorption spectra of chrysene and 1,2,7,8 dibenzanthracene," *Chemical Physics Letters*, vol. 12, no. 2, pp. 281–284, 1971.
- [5] J. P. Larkindale and D. J. Simkin, "Magnetic circular dichroism of the α bands of some polycyclic aromatic hydrocarbons," *The Journal of Chemical Physics*, vol. 55, no. 12, pp. 5668–5674, 1971.
- [6] D. Lavalette, C. J. Werkhoven, D. Deblaar, J. Langelaar, and J. D. W. Van Voorst, "Excited singlet state polarization and absorption spectra of 1,2-benzocoronene, 1,12-benzperylene and 1,2:3,4-dibenzanthracene," *Chemical Physics Letters*, vol. 9, no. 3, pp. 230–233, 1971.
- [7] G. P. Barnett, M. A. Kurzmack, and M. M. Malley, "Polarizability changes in certain condensed aromatic hydrocarbons," *Chemical Physics Letters*, vol. 23, no. 2, pp. 237–240, 1973.

- [8] M. A. Silifkin and A. O. Al-Chalabi, "Modulation excitation spectra of some aromatic hydrocarbons at high concentration, evidence for triplet excimer formation," *Chemical Physics Letters*, vol. 29, no. 1, pp. 110–112, 1974.
- [9] R. G. E. Morales and G. Traverso, "Indirect determination of electronic transition frequencies of coronene, triphenylene and 1,2,5,6-dibenzanthracene in the vapor phase," *Spectroscopy Letters*, vol. 15, no. 8, pp. 623–629, 1982.
- [10] O. Schafer, M. Allan, E. Haselbach, and R. S. Davidson, "Triplet energies and electron affinities of methyl-acrylate and methyl-methacrylate," *Photochemistry and Photobiology*, vol. 50, no. 6, pp. 717–719, 1989.
- [11] F. Bayrakceken, "A new type of delayed fluorescence of rubrene in solution," *Journal of Luminescence*, vol. 54, no. 1, pp. 29–33, 1992.
- [12] F. Bayrakceken, B. Baris, O. J. Demir, and A. Cavus, "B-type delayed fluorescence of rubreneperoxide in solution," *Spectroscopy Letters*, vol. 29, no. 1, pp. 151–157, 1996.
- [13] M. S. Deleuze, "Valence one-electron and shake-up ionisation bands of polycyclic aromatic hydrocarbons. IV. The dibenzanthracene species," *Chemical Physics*, vol. 329, no. 1–3, pp. 22–38, 2006.
- [14] M. Gussonia, M. Ruib, and G. Zerbi, "Electronic and relaxation contribution to linear molecular polarizability. An analysis of the experimental values," *Journal of Molecular Structure*, vol. 447, no. 3, pp. 163–215, 1998.
- [15] T. Vo-Dinh, J. Fetzer, and A. D. Campiglia, "Monitoring and characterization of polyaromatic compounds in the environment," *Talanta*, vol. 47, no. 4, pp. 943–969, 1998.
- [16] F. P. Guengerich, "Forging the links between metabolism and carcinogenesis," *Mutation Research*, vol. 488, no. 3, pp. 195–209, 2001.
- [17] A. D. Boney and E. D. S. Corner, "On the effects of some carcinogenic hydrocarbons on the growth of sporelings of marine red algae," *Journal of the Marine Biological Association of the United Kingdom*, vol. 42, no. 3, pp. 579–585, 1962.
- [18] R. R. Arnaiz and G. O. Téllez, "Structure-activity relationships of several anisidine and dibenzanthracene isomers in the w/w+ somatic assay of *Drosophila melanogaster*," *Mutation Research*, vol. 514, no. 1-2, pp. 193–200, 2002.
- [19] C. Heidelberger, M. E. Baumann, L. Griesbach, A. Ghobar, and T. M. Vaughan, "The carcinogenic activities of various derivatives of dibenzanthracene," *Cancer Research*, vols. 22, pp. 78–83, 1962.

Research Article

Resonance Fluorescence of Fused Silica by the Depopulation of the Ground State

Fuat Bayrakceken¹ and Korkut Yegin²

¹ Department of Biomedical Engineering, Yeditepe University, Istanbul, Turkey

² Department of Electrical and Electronics Engineering, Yeditepe University, Istanbul, Turkey

Correspondence should be addressed to Korkut Yegin, kyegin@yeditepe.edu.tr

Received 30 May 2012; Accepted 10 October 2012

Academic Editor: Ipek Karaaslan

Copyright © 2012 F. Bayrakceken and K. Yegin. This is an open access article distributed under the Creative Commons Attribution License, which permits unrestricted use, distribution, and reproduction in any medium, provided the original work is properly cited.

Spectroscopically pure fused silica has been used in many applications ranging from optoelectronics and optical fibers to laser flash spectroscopy. Although ultraviolet light irradiated optical absorption spectra and coherence fluorescence of silicon dioxide have been studied in the past, we present discrete absorption and resonance coherent fluorescence line of silicon dioxide which were recorded photographically at 288.2 nm. This discrete fluorescence is observed at room temperature using high photon flux (10^{24} photon/pulse) excitation spectroscopy.

1. Introduction

Resonance fluorescence occurs when atoms/molecules absorb and reemit radiation at the same wavelength. Resonance fluorescence line corresponds to the transition between an electronic excited state and the ground state. The wavelengths of the absorption (λ_A) and fluorescence (λ_F) are the same for resonance transitions. Resonance fluorescence process of silicon dioxide is shown in Figure 1.

Coherent resonance fluorescence and ultraviolet (UV) light induced optical absorption spectra were reported in [1] and resonance fluorescence was observed in the 250–255 nm band at room temperature by high photon flux excitation spectroscopy. As discussed in previous works [1–7], fused silica exhibits coherent fluorescence in the ultraviolet C region (UV-C).

UV grade fused silica is an amorphous form of silicon dioxide made from flame hydrolysis of silicon tetrachloride. On top of high UV transmission, it has the properties of low thermal expansion coefficient and high laser damage threshold. Amorphous fused silica form bonds in definite vectorial positions in space such that ring structures that connect molecules can exist [8, 9]. A random network of atoms in fused silica was shown in [10] and reproduced

in Figure 2. Ring structures consist of tetrahedral atomic arrangements and most ring structures contain five or six ring members simply because the bond angle between O–Si–O permits formation of almost perfect tetrahedrons with less strain energy.

The vibrational level patterns for silicon dioxide are not complex for six- or eight rings, which, in turn, enables one to observe transitions in 250–255 nm band as discrete narrow bands [1]. The bandwidths of these coherent emissions were reported approximately 1/25 nm in [1]. These narrow absorption and emission lines are reproduced from [1] with the permission Bayrakceken and shown in Figure 3.

Apart from these reported discrete absorption and fluorescence of fused silica, a single line at 288.2 nm without any vibrational and/or rotational bands was also observed in our experiments and this is shown in Figure 4.

This discrete line at 288.2 nm was observed previously and investigated in the context of Raman resonance scattering and it was stated that only one absorption band was observed at 288.2 nm, seven anti-Stokes lines at 285–288.2 nm and nine Stokes lines at 288.2–290 nm band [3]. However, in our experiments, we observed a single-line coherent emission although the UV irradiation was performed on a molecule. This may be due to different

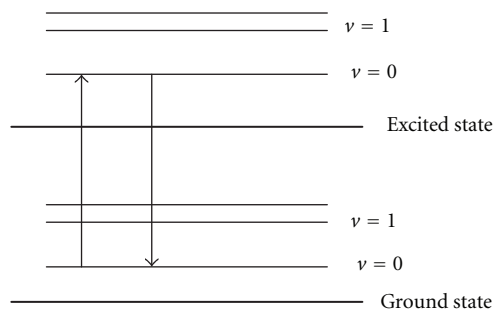


FIGURE 1: Resonance fluorescence of SiO₂.

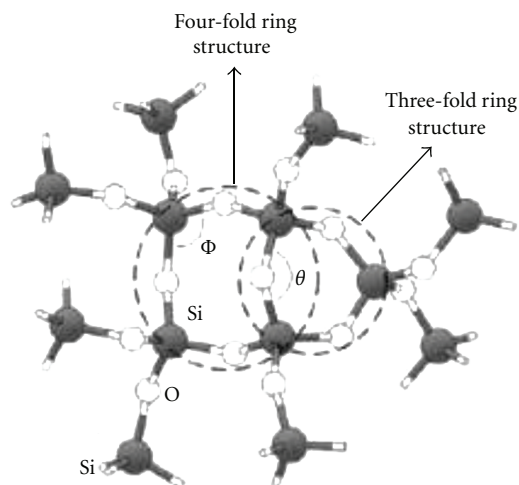


FIGURE 2: Ball and stick model of fused silica in random network (encircled are three-fold and four-fold ring structures) (reproduced from [10]).

photon flux densities used in the studies. The photographic image of the resonance fluorescence line shown in Figure 4 was recorded for the first time.

2. Material and Methods

Spectroscopically pure fused silica (Corning Glass Co.), reagent-grade material, was selected for absorption and luminescence experiments. A flash photolysis setup consisting of two parallel phototubes in series, contained in a reflector (front surface mirrored, reflecting the 200–700 nm band of electromagnetic radiation), was used for the excitation of fused silica sample. The entire optical pumping cavity was flushed with oxygen-free nitrogen to eliminate the presence of paramagnetic oxygen in the optical pumping system. Photoflash energies in the range of 780–1125 J were used and the flash duration time ($1/e$ time) of the optical pumping device was $2 \mu\text{s}$. Hilger medium quartz spectrograph with slit width 0.025 mm was used for the recordings of absorption, emission, and lasing spectra. Ilford XK fast blue sensitive plates from Kodak, sensitized with sodium salicylate for UV-C region recordings were developed in Ilford PQ universal developer. Joyce-Loebel MKIIB double-beam recording mirror densitometer was

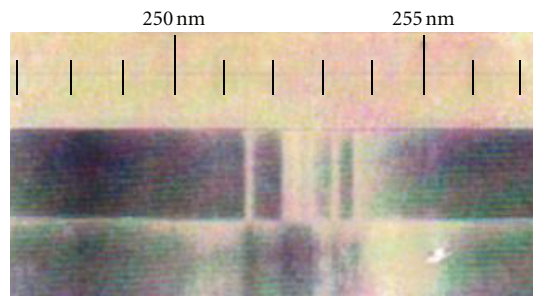


FIGURE 3: Optical discrete absorption and resonance fluorescence of fused silica in the UV (reproduced from [1]).

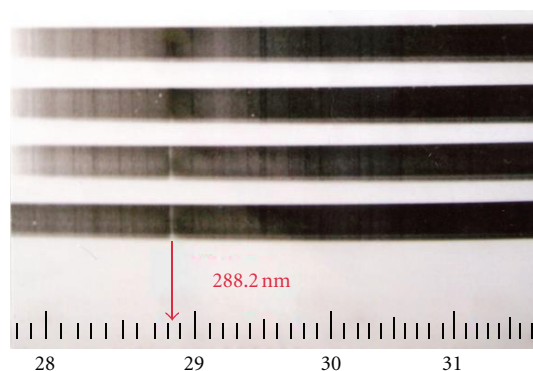


FIGURE 4: Discrete absorption and resonance fluorescence lines of silicon dioxide at 288.2 nm.

used for photometered spectra. Single flashes were utilized for all spectroscopic recordings.

3. Results and Discussion

It is well known that absorption of UV light in the UV-C raises fused silica from the ground state to several excited states. At room temperature, most of the molecules are in the lowest vibrational level of the ground state ($v=0$) and transitions to higher levels will take place with the absorption of UV light. For silicon dioxide, the vibrational levels are not complex. In fact, symmetric stretching, symmetric bending, and antisymmetric stretching are the only normal modes of SiO₂ and these can be observed in the infrared region because electric dipole transitions occur only for normal modes and they are infrared active. The infrared absorption band of SiO₂ has been extensively studied in the past [11, 12]. In the UV region of the spectrum, the interaction of the electromagnetic radiation with electrons in Si–O bonds, structural imperfections, Si–Si bonds cause strong absorption [13–15]. These lead to sharp UV cut-off around 160 nm [12–15]. The location of the absorption edge naturally depends on the composition, impurity level, structural defects, and temperature. Experimental spectroscopic data between 90 and 350 nm have been presented in [14].

In general, the bandwidths of normal (prompt) fluorescence are narrower than the corresponding absorption bands due to the dispersion associated with the structure

during emission. However, if the fluorescence emissions are coherent, the integrated areas under the absorption bands and coherent super-imposed fluorescence emissions will become equal, which, in turn, enables full depopulation of ground state, and all emission transitions will be resonance fluorescence as shown in Figures 3 and 4. The fluorescence radiance can be expressed as follows:

$$B_F = \frac{l}{4\pi} Y_{21} E_{\nu_{12}} \int_0^{\infty} k_{\nu} d\nu, \quad (1)$$

where B_F is absolute radiance l is the path length, Y_{21} is power efficiency (due to quenching) $W_{\text{fluoresced}}/W_{\text{absorbed}}$, $E_{\nu_{12}}$ is the spectral irradiation of source at absorption line frequency of ν_{12} , and k_{ν} is the absorption coefficient. The integration term provides the integrated absorption coefficient over the absorption line, which is a function of the concentration of ground and excited states.

4. Conclusion

We note that no additional fluorescence and/or scattering were observed in lower bands, that is, 270–275 nm. Moreover, all spectral and lasing emissions were recorded at room temperature. Therefore, we also argue that the population inversion and the depopulation of ground state are permissible. As shown in Figure 4, resonance fluorescence at 288.2 nm was very intense and coherent. Thus, it is possible to use fused silica as a laser material in the UV or as a UV detector with its inherent visible-blind property.

References

- [1] F. Bayrakçeken, "Sensitive detection of optical discrete absorption and lasing of fused silica by the depopulation of the ground state," *Applied Physics B*, vol. 105, pp. 573–574, 2011.
- [2] F. Bayrakçeken, A. Yaman, and B. B. Jomehri, "Resonance fluorescence studies of spectroscopically pure SiO₂," *Journal of the Indian Chemical Society*, vol. 77, no. 9, pp. 445–446, 2000.
- [3] A. Yaman, A. B. Bayrakçeken, O. J. Demir, and F. Bayrakçeken, "Electronic absorption and Raman resonance scattering of spectroscopically pure SiO₂," *Spectrochimica Acta A*, vol. 56, no. 10, pp. 1901–1903, 2000.
- [4] S. Hayashi and K. Yamamoto, "Optical properties of Si-rich SiO₂ films in relation with embedded Si mesoscopic particles," *Journal of Luminescence*, vol. 70, pp. 352–363, 1996.
- [5] Y. Sakurai and K. Nagasawa, "Green photoluminescence band in γ -irradiated oxygen-surplus silica glass," *Journal of Applied Physics*, vol. 86, article 1377, 5 pages, 1999.
- [6] A. Teramoto, K. Kobayashi, Y. Ohno, and A. Shigetomi, "Excess currents induced by hot hole injection and FN electron injection in thin SiO₂ films," *IEEE Transactions on Electron Devices*, vol. 48, no. 5, pp. 868–873, 2001.
- [7] A. Anedda, C. M. Carbonaro, R. Corpino, and A. Serpi, "Vacuum ultraviolet absorption of silica samples," *Journal of Non-Crystalline Solids*, vol. 245, pp. 183–189, 1999.
- [8] S. V. King, "Ring configurations in a random network model of vitreous silica," *Nature*, vol. 213, no. 5081, pp. 1112–1113, 1967.
- [9] J. P. Reno and I. Ebbsjo, "Structure of rings in vitreous SiO₂," *Physical Review B*, vol. 47, pp. 3053–3062, 1993.
- [10] S. Vukelic, S. Ryu, B. Gao, and Y. L. Yao, "Structural modification of amorphous fused silica under femtosecond laser irradiation," in *Proceedings of the ASME International Manufacturing Science and Engineering Conference (MSEC '08)*, pp. 227–236, October 2008.
- [11] A. M. Efimov, *Optical Constants of Inorganic Glasses*, CRC Press, Boca Raton, Fla, USA, 1995.
- [12] I. Fanderlik, *Optical Properties of Glass*, vol. 5 of *Glass Science and Technology*, Elsevier Science, New York, NY, USA, 1983.
- [13] K. Kajihara, "Improvement of vacuum-ultraviolet transparency of silica glass by modification of point defects," *Journal of the Ceramic Society of Japan*, vol. 115, no. 1338, pp. 85–91, 2007.
- [14] G. H. Siegel, "Ultraviolet spectra of silicate glasses: a review of some experimental evidence," *Journal of Non-Crystalline Solids*, vol. 13, no. 3, pp. 372–398, 1974.
- [15] N. Shimodaira, K. Saito, A. J. Ikushima, T. Kamihori, and S. Yoshizawa, "VUV transmittance of fused silica glass influenced by thermal disorder," in *Proceedings of the 13th Optical Microlithography*, vol. 4000 of *Proceedings of SPIE*, pp. 1553–1559, March 2000.

Research Article

Thin Films Prepared from Nanometer Size TiO₂ Absorbs Millimeter Waves

Mehmet Ali Yesil,¹ Korkut Yegin,¹ Mustafa Culha,² and Esen Efeoglu²

¹ Department of Electrical and Electronics Engineering, Yeditepe University, Istanbul 34755, Turkey

² Department of Genetics and Bioengineering, Yeditepe University, Istanbul 34755, Turkey

Correspondence should be addressed to Mehmet Ali Yesil, mehmetaliyesil.07@gmail.com

Received 27 July 2012; Accepted 10 October 2012

Academic Editor: Ipek Karaaslan

Copyright © 2012 Mehmet Ali Yesil et al. This is an open access article distributed under the Creative Commons Attribution License, which permits unrestricted use, distribution, and reproduction in any medium, provided the original work is properly cited.

Absorption of average 10 nm size TiO₂ nanoparticles deposited on glass surfaces as a thin film using convective assembly technique and drop-casting is studied in the millimeter wave range from 26 GHz to 40 GHz. The millimeter wave responses of the fabricated samples were obtained using a vector network analyzer. Reflection properties of the prepared samples were also measured. Absorption and reflection of TiO₂ nanoparticles were more pronounced between 35 GHz and 40 GHz compared to glass-only sample.

1. Introduction

Titanium dioxides find broad range of applications from pigment to cosmetic industry, electronic to pharmaceutical industry [1–10]. The reason behind their wide applicability is their unique properties such as blocking UV light and photocatalytic activity [11]. Additional exceptional properties such as cleaving proteins at amino acid proline site and behaving as a semiconductor of nanosized TiO₂ were also reported [12, 13].

As the nanotechnology progresses, new properties of TiO₂, especially in their nanoscale form, are explored. For example, the millimeter wave rotational spectrum of TiO₂ at ground state was obtained in [14] for astronomical searches. Microwave absorbing effects and characterization of TiO₂ were also studied in [15, 16]. The absorption characteristics of TiO₂ nanoparticles have been mostly overlooked and this study aims to fill this gap for numerous engineering applications.

There are a number of methods such as spin coating, dip coating, and drop-casting to prepare relatively uniform thin films from nanomaterials. In this study, we used two different approaches to prepare TiO₂ thin films, drop-casting and “convective assembly”. While former approach generates thin film thickness in millimeter range, the latter generates

in the micrometer range. The “convective assembly” is an approach to assemble 2D and 3D nano- and micrometer size structures using nano- and micrometer size particles on surfaces in a more controlled manner. The assembly of a number of particles on surfaces was achieved using the approach [17, 18]. The self-assembly of colloidal particles in thin evaporating films is the basis of the technique [19, 20]. It was also used to assemble bacteria-silver nanoparticle and protein-silver nanoparticle structures on glass surfaces [21, 22].

2. Material and Methods

10 nm TiO₂ nanoparticles were used to prepare thin films on glass surfaces. Figure 1(a) shows the TEM images of TiO₂. As seen on the image, the average size of TiO₂ nanoparticles is 10 nm. An 8.6 mg of TiO₂ was suspended in distilled water. A “convective assembly” was used to deposit TiO₂ as a thin film on a glass surface. The details of the experimental setup could be found elsewhere [17]. Briefly, an 80 μL of TiO₂ suspension was placed at the cross section of two glass slides, which are soaked in Piranha solution for at least 3 hours to clean the glass surface, one is placed on a moving stage and the other is placed on top of the one placed on the moving stage with an angle of 23°. In order to generate

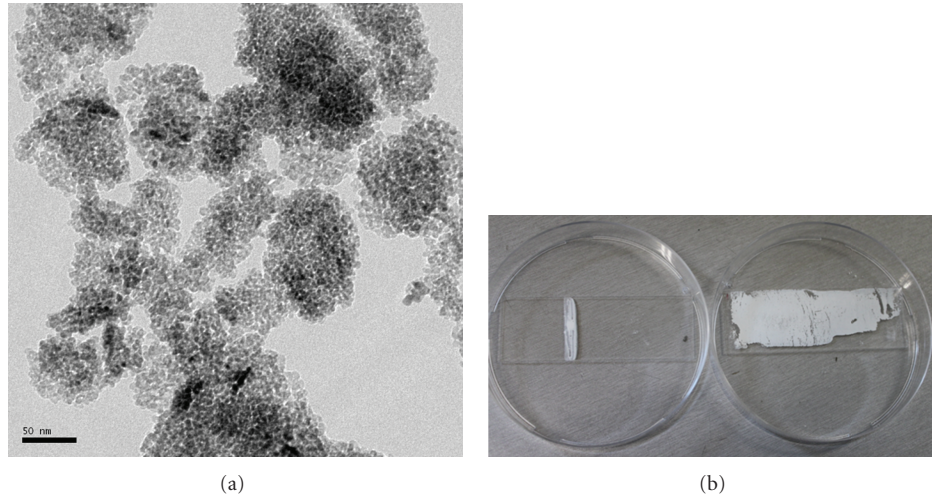


FIGURE 1: (a) TEM image of TiO_2 nanoparticles, (b) thin films prepared on glass surfaces using convective assembly and drop-casting.

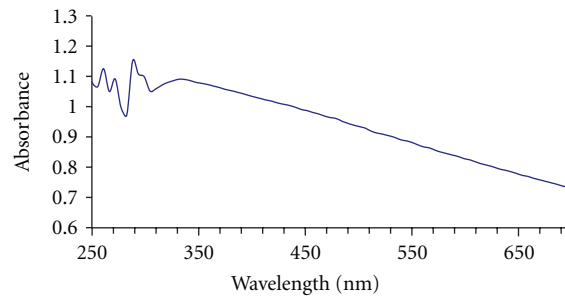


FIGURE 2: UV/Vis spectrum of fabricated nanoparticles in water.

thicker films on the glass surface, 4–6 mL of suspension of TiO_2 was placed on the glass cleaned glass slide and the suspension was distributed on the glass surface with the help of another slide. Figure 1(b) shows the images of thin films prepared with two different approaches on the glass surface. The thickness of thin film prepared with convective assembly estimated as $10\ \mu\text{m}$ and the film prepared with drop-casting was estimated as 1 mm.

Figure 2 shows the UV/Vis spectrum of the suspension of TiO_2 nanoparticles in water.

Millimeter wave measurement setup is shown in Figure 3. Rohde and Schwarz ZVA40 Network Analyzer was calibrated from 20 to 40 GHz with intermediate frequency at 1 kHz, and the number of calibration points was set to 10,000 with source power level at +5 dBm. Network Analyzer as a two-port device can simultaneously measure input reflection and transmission to the other port in terms of Scattering (S) parameters. In this configuration S_{21} represents signal received at port 2 when input signal is applied to port 1, with 50 Ohm port impedances. S_{21} is used as the main data for comparison of detection. Wideband conical antennas made by Elmika were used for transmission and reception. Although the antennas were rated from 26.5 to 40 GHz, their port match and gain were found satisfactory starting from 23 GHz. Nevertheless, measurements were carried out

relative to glass-only sample, and basis of comparison was made with reference to that sample. Samples were held using Rohacell air-dielectric foams.

3. Results and Discussion

Measurement setup was first used for free space and thin-glass samples to create a reference. Transmission measurement of S_{21} is recorded for both configurations. Since the samples are in the far field of the receiving and transmitting antennas and reflection from the samples is quite close to each other, one can infer absorption of samples directly from transmission measurements. Comparisons of transmission measurements for free space and glass-only sample are shown in Figure 4. The measurement result is also expressed in dB scale with $20\log(S_{21})$ conversion.

Next, same measurement setup was used to measure absorption characteristics on TiO_2 thin films deposited on glass surface using drop-casting technique. The samples prepared using convective assembly were very thin to produce strong absorption. Therefore, samples prepared through drop-casting were used in the measurements. Results are shown in Figure 5. It is observed that there is a degradation TiO_2 deposited glass sample compared to glass-only sample.

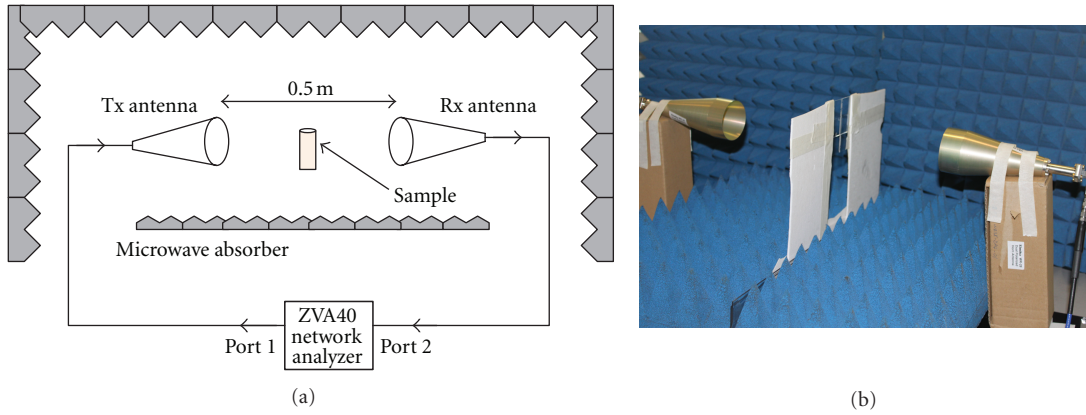


FIGURE 3: Measurement setup, (a) description, (b) picture of the setup.

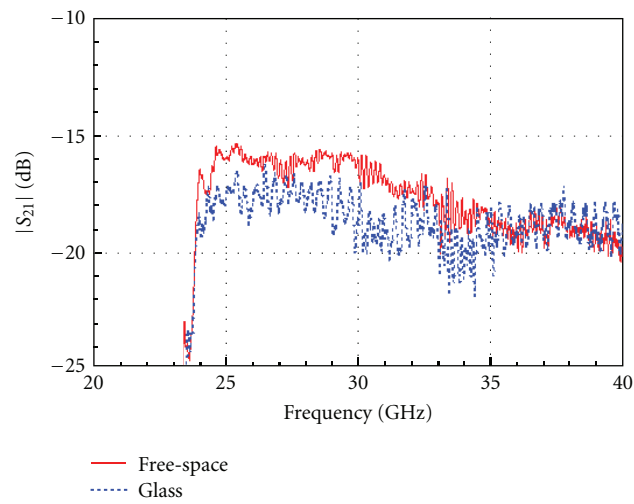


FIGURE 4: Transmission measurements of free-space and glass-only sample.

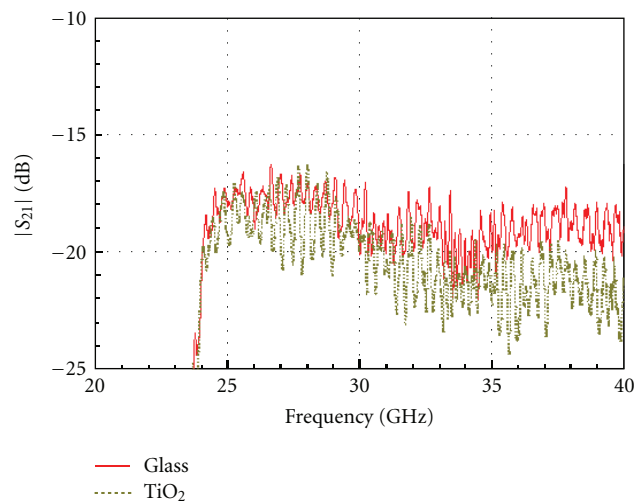


FIGURE 5: Transmission measurements of TiO_2 deposited glass and glass-only samples.

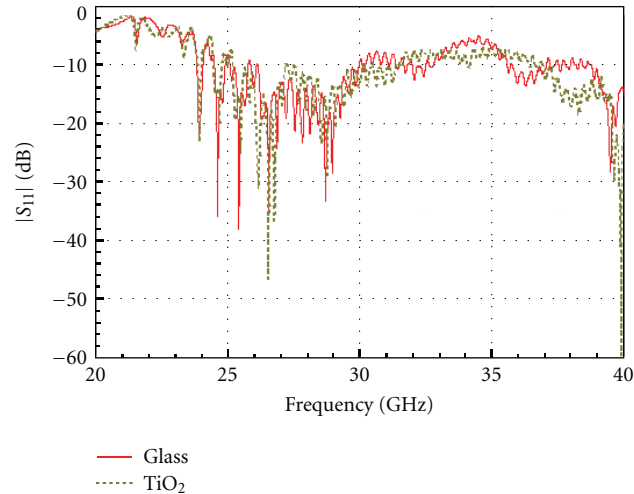


FIGURE 6: Reflection measurements of TiO_2 deposited glass and glass-only samples.

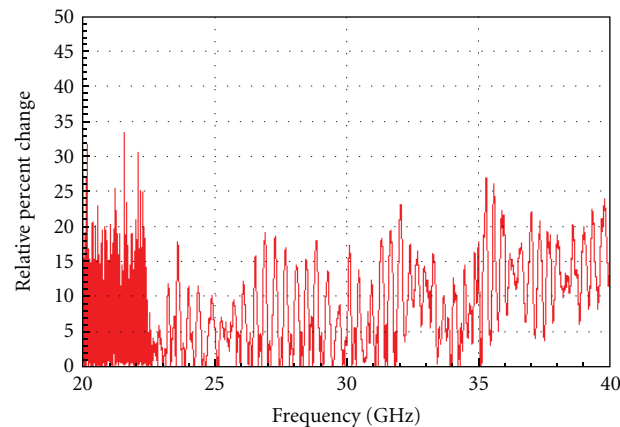


FIGURE 7: Relative percent change of TiO_2 sample with reference to glass-only sample.

Especially between 35 GHz to 40 GHz, absorption of TiO_2 sample is at least 2.5 to 3 dB higher than that of glass-only sample. The reflection measurements of both samples are also shown in Figure 6. The reflection measurements also show a clear departure from glass-only sample from 35 GHz to 40 GHz.

The relative percent change in received signal with respect to glass-only sample is shown in Figure 7. TiO_2 sample has in excess of 15% relative percent change from 35 to 40 GHz.

Even though the measurements were carried out at atmospheric pressures and at room temperature, there is a clear difference between glass-only and TiO_2 thin film deposited glass samples. The attenuation of TiO_2 sample is consistently higher than that of glass-only sample.

References

- [1] M. Ramovatar, R. Madhu, P. Ruchita et al., "Nano- TiO_2 -induced apoptosis by oxidative stress-mediated DNA damage and activation of p53 in human embryonic kidney cells," *Applied Biochemistry and Biotechnology*, vol. 167, no. 4, pp. 791–808, 2012.
- [2] M. Valeria and C. Ilaria, "Toxic effects of engineered nanoparticles in the marine environment: model organisms and molecular approaches," *Marine Environmental Research*, vol. 76, pp. 32–40, 2012.
- [3] M. S. Kim, D. M. Chun, J. O. Choi et al., "Room temperature deposition of TiO_2 using nano particle deposition system (NPDS): application to dye-sensitized solar cell (DSSC)," *International Journal of Precision Engineering and Manufacturing*, vol. 12, no. 4, pp. 749–752, 2011.
- [4] B. J. Shaw and R. D. Handy, "Physiological effects of nanoparticles on fish: a comparison of nanometals versus metal ions," *Environment International*, vol. 37, no. 6, pp. 1083–1097, 2011.
- [5] C. Som, P. Wick, H. Krug, and B. Nowack, "Environmental and health effects of nanomaterials in nanotextiles and façade coatings," *Environment International*, vol. 37, no. 6, pp. 1131–1142, 2011.
- [6] K. M. Tyner, A. M. Wokovich, D. E. Godar, W. H. Doub, and N. Sadrieh, "The state of nano-sized titanium dioxide (TiO_2) may affect sunscreen performance," *International Journal of Cosmetic Science*, vol. 33, no. 3, pp. 234–244, 2011.

- [7] F. A. Babakhani, A. R. Mehrabadi, P. N. L. Lens, and M. Sadatian, "Prevention of biofilm formation in water and wastewater installations by application of TiO₂ nano particles coating," *Desalination and Water Treatment*, vol. 28, no. 1–3, pp. 83–87, 2011.
- [8] C. Cherchi, T. Chernenko, M. Diem, and A. Z. Gu, "Impact of nano titanium dioxide exposure on cellular structure of anabaena variabilis and evidence of internalization," *Environmental Toxicology and Chemistry*, vol. 30, no. 4, pp. 861–869, 2011.
- [9] C. C. Lin and W. J. Lin, "Sun protection factor analysis of sunscreens containing titanium dioxide nanoparticles," *Journal of Food and Drug Analysis*, vol. 19, no. 1, pp. 1–8, 2011.
- [10] M. Hassan Marwa, N. Mohammad Louay, B. Cooper Samuel III et al., "Evaluation of nano-titanium dioxide additive on asphalt binder aging properties," *Transportation Research Record*, vol. 2207, pp. 11–15, 2011.
- [11] M. E. Kurtoglu, T. Longenbach, and Y. Gogotsi, "Preventing sodium poisoning of photocatalytic TiO₂ films on glass by metal doping," *International Journal of Applied Glass Science*, vol. 2, no. 2, pp. 108–116, 2011.
- [12] B. J. Jones, M. J. Vergne, D. M. Bunk, L. E. Locascio, and M. A. Hayes, "Cleavage of peptides and proteins using light-generated radicals from titanium dioxide," *Analytical Chemistry*, vol. 79, no. 4, pp. 1327–1332, 2007.
- [13] R. Paschotta, "Bragg mirrors," in *Encyclopedia of Laser Physics and Technology*, 2009.
- [14] P. Kania, M. Hermanns, S. Brünken, H. S. P. Müller, and T. F. Giesen, "Millimeter-wave spectroscopy of titanium dioxide, TiO₂," *Journal of Molecular Spectroscopy*, vol. 268, no. 1-2, pp. 173–176, 2011.
- [15] S. Horikoshi, A. Matsubara, S. Takayama et al., "Characterization of microwave effects on metal-oxide materials: zinc oxide and titanium dioxide," *Applied Catalysis B*, vol. 99, no. 3-4, pp. 490–495, 2010.
- [16] L. B. Zhang, G. Chen, J. H. Peng, J. Chen, S. H. Guo, and X. H. Duan, "Microwave absorbing properties of high titanium slag," *Journal of Central South University of Technology*, vol. 16, no. 4, pp. 588–593, 2009.
- [17] M. Culha, M. Muge Yazıcı, M. Kahraman, F. Sahin, and S. Kocagoz, "Surface-enhanced raman scattering of bacteria in microwells constructed from silver nanoparticles," *Journal of Nanotechnology*, vol. 2012, Article ID 297560, 7 pages, 2012.
- [18] C. E. Ashley, D. R. Dunphy, Z. Jiang et al., "Convective assembly of 2D lattices of virus-like particles visualized by in-situ grazing-incidence small-angle X-ray scattering," *Small*, vol. 7, no. 8, pp. 1043–1050, 2011.
- [19] N. D. Denkov, O. D. Velev, P. A. Kralchevsky, I. B. Ivanov, H. Yoshimura, and K. Nagayama, "Mechanism of formation of two-dimensional crystals from latex particles on substrates," *Langmuir*, vol. 8, no. 12, pp. 3183–3190, 1992.
- [20] N. D. Denkov, O. D. Velev, P. A. Kralchevsky, I. B. Ivanov, H. Yoshimura, and K. Nagayama, "Two-dimensional crystallization," *Nature*, vol. 361, no. 6407, p. 26, 1993.
- [21] M. Kahraman, M. M. Yazici, F. Şahin, and M. Çulha, "Convective assembly of bacteria for surface-enhanced Raman scattering," *Langmuir*, vol. 24, no. 3, pp. 894–901, 2008.
- [22] S. Keskin, M. Kahraman, and M. Çulha, "Differential separation of protein mixtures using convective assembly and label-free detection with surface enhanced Raman scattering," *Chemical Communications*, vol. 47, no. 12, pp. 3424–3426, 2011.

Research Article

Fluorescence, Decay Time, and Structural Change of Laser Dye Cresyl Violet in Solution due to Microwave Irradiation at GSM 900/1800 Mobile Phone Frequencies

Fuat Bayrakceken¹ and Korkut Yegin²

¹ Department of Biomedical Engineering, Yeditepe University, 34755 Istanbul, Turkey

² Department of Electrical and Electronics Engineering, Yeditepe University, 34755 Istanbul, Turkey

Correspondence should be addressed to Korkut Yegin, kyegin@yeditepe.edu.tr

Received 24 May 2012; Accepted 3 October 2012

Academic Editor: Necdet Aslan

Copyright © 2012 F. Bayrakceken and K. Yegin. This is an open access article distributed under the Creative Commons Attribution License, which permits unrestricted use, distribution, and reproduction in any medium, provided the original work is properly cited.

Microwave irradiation at GSM 900/1800 MHz mobile phone frequencies affects the electronic structure of cresyl violet in solution. These changes are important because laser-dye cresyl violet strongly bonds to DNA- and RNA-rich cell compounds in nerve tissues. The irradiation effects on the electronic structure of cresyl violet and its fluorescence data were all obtained experimentally at room temperature. For most laser dyes, this is not a trivial task because laser dye molecules possess a relatively complex structure. They usually consist of an extended system of conjugated double or aromatic π -bonds with attached auxochromic (electron donating) groups shifting the absorption band further towards longer wavelength. Because of the intrinsically high degree of conjugation, the vibrational modes of the molecular units couple strongly with each other. We found that the fluorescence quantum yield was increased from 0.54 ± 0.03 to 0.75 ± 0.01 due to intramolecular energy hopping of cresyl violet in solution which is exposed to microwave irradiation at mobile phone frequencies, and the photonic product cannot be used as a laser dye anymore.

1. Introduction

Cresyl violet (Figure 1) is often used as a staining agent for studying the changes on DNA- and RNA-rich compounds in tissues. Especially, the effects of microwave radiation on blood-brain barrier permeability heavily rely on cresyl violet based stain analysis, simply because laser dye molecules are often distinguished due to their relatively complex structure in photoluminescence data. However, effects of microwave irradiation on cresyl violet in solution have not been studied in detail, and changes in the absorption band due to microwave irradiation are particularly important for widespread applications of laser dye cresyl violet.

The photophysical and chemical behaviors of cresyl violet are strongly influenced by electrostatic, hydrogen-bond, and acid-base interactions in solution, as well as by its hydrophobicity [1]. The rotational relaxation of a solute molecule depends on its environment, especially for the case of ionic and polar solute species embedded in electrolyte

solutions [2–5]. In such cases, solute-solvent electrostatic interactions can significantly influence the behavior of the solute. Dramatic changes in the local solvent structure and the solute dynamics occur for ionic solute molecules. Laser dyes are organic compounds that relax radiatively after optical excitation, emitting in the UV-visible or IR range [6]. Today a large variety of luminescent dyes have been optimized for use in circulating liquid lasers. These dyes have a range of practical applications when rigidized in a polymer host. One area that may be revolutionized by the use of organic luminophores in plastics is the flat-screen monitor industry. Organic emitters doped in a polymer layer offer an inexpensive, malleable, and easy-to-produce alternative. Organic dyes are also of interest for sensors, optical amplifiers, and fiber optics. Unfortunately, upon repeated absorption the laser dye molecules begin to photooxidize and cresyl violet becomes an emitter at four different wavelengths. It is stable under ambient conditions with minimal light power saturation even at peak intensities

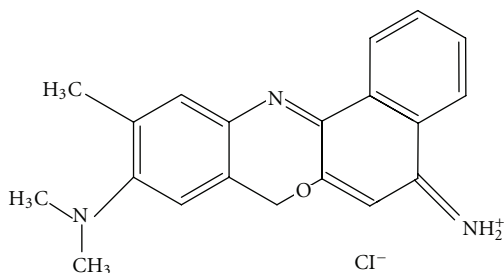


FIGURE 1: Molecular structure of cresyl violet.

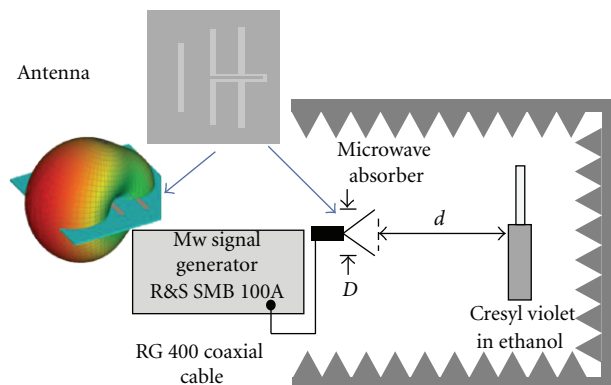


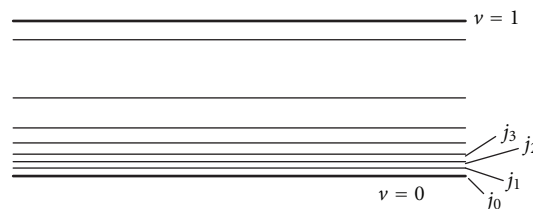
FIGURE 2: microwave irradiation set up, antenna configuration (front and back), and antenna radiation pattern.

as high as 100 MW/cm^2 where its molecular weight is 361.74 g/mol .

Our experiment consisted of irradiating cresyl violet in solution which was doped in thin solid slabs of polymethylmethacrylate with progressively higher intensities of light tuned to an absorption peak of cresyl violet molecule for photobleaching experiments. The calculated wavenumbers of the normal modes are in good agreement with our experimental values. Some of the characteristic vibrational modes of cresyl violet were given [7]. The correlation between effective dipole moments change of the guest molecule and the hole-burning efficiencies of the host matrices illustrates the sensitivity of the dipole moment change as a direct measure of guest-host interactions. The effective dipole moment change of cresyl-violet-perchlorate ranges from 0.14 to 0.59 Debye [8–10].

2. Materials and Methods

Cresyl violet, was of Aldrich reagent grade, used as received without any further purification. All other chemicals were also of reagent grade. Cresyl violet, at a concentration of $2 \times 10^{-5} \text{ M}$, was in ethanol at room temperature. Ocean Optics spectrophotometer was used for recording absorption spectra. The singlet and triplet transient phenomena were excited with a laser flash photolysis setup consisting of a Q-switched and mode-locked Nd:YAG laser system at 532 nm (300 mJ) and at 1064 nm (1 J). A kinetic absorption spectrophotometer with nanosecond response (pulsed

FIGURE 3: Illustration of rotational states as sublevels of $v = 0$ state.

with 500 W Xenon lamp), Bausch and Lomb UV-visible high-intensity monochromator, RCA-4840 photomultiplier tube with output signal terminated into 93Ω Tektronix 7912 digitizer, and an LSI-11 microprocessor unit which controlled the experiments and processed the data at the initial stage, were used. The flash photolysis experiments were carried out with oxygen-free nitrogen, degassed in the high vacuum system (vacuum line background pressure was 10^{-7} Torr) and contained in $1 \times 0.2 \text{ cm}^2$ quartz cells with the absorbed light passing along the 0.2 cm path length. The exciting laser beam intersected the cell at angles ranging from 20° – 90° , and the flash duration time was $3.0 \pm 0.1 \text{ ns}$.

The microwave irradiation frequencies for the cresyl violet in ethanol are chosen as 925 MHz , center frequency of GSM 900 (890 – 960 MHz) and 1940 MHz , center frequency of GSM 1800/1900 and 3G frequency band (1710 – 2170 MHz). Frequencies are not applied at the same time, but rather half of the target duration with 925 MHz and the other half with 1940 MHz . Although cellular phone communication utilizes pulsed transmissions in a time-shared manner, we applied continuous wave (CW) with no signal modulation in our experiments. This deviation from real-life application does not affect current analysis as irradiation effects rather than interference effects are scrutinized. CW power level is set to 30 dBm (1 W) using Rohde-Schwarz SMB 100A signal generator. An antenna is connected to the signal generator with microwave coaxial cable, RG400A to transmit microwave energy to the solution. A balanced type, three-element (reflector, driver, and director) directional printed dipole Yagi antenna is designed at 1940 MHz . The same antenna works well at 925 MHz also with a bit sacrifice on impedance match. Also, the antenna has an integrated quarter-wavelength Marchand balun (balanced to unbalanced) to minimize the coupling between the antenna and the measurement cable and to reduce the loading effects of the sample on the antenna. The antenna geometry and the integrated balun are designed with a 3D electromagnetic field solver. Although the computed total gain (vertical and horizontal) at its principal axis of the antenna is 5.73 dBi (relative to isotropic source) at 1940 MHz , near-field (beyond reactive zone) electric field illumination at the solution is important. The antenna input impedance is matched to that of the signal generator, which is 50Ω . The antenna is built on a low-cost, two-sided FR4 substrate with 1.57 mm standard thickness and its one-port characteristics are measured with Rohde-Schwarz ZVB20 network analyzer. The shape of the antenna (front and back), 3D far-field pattern, and the

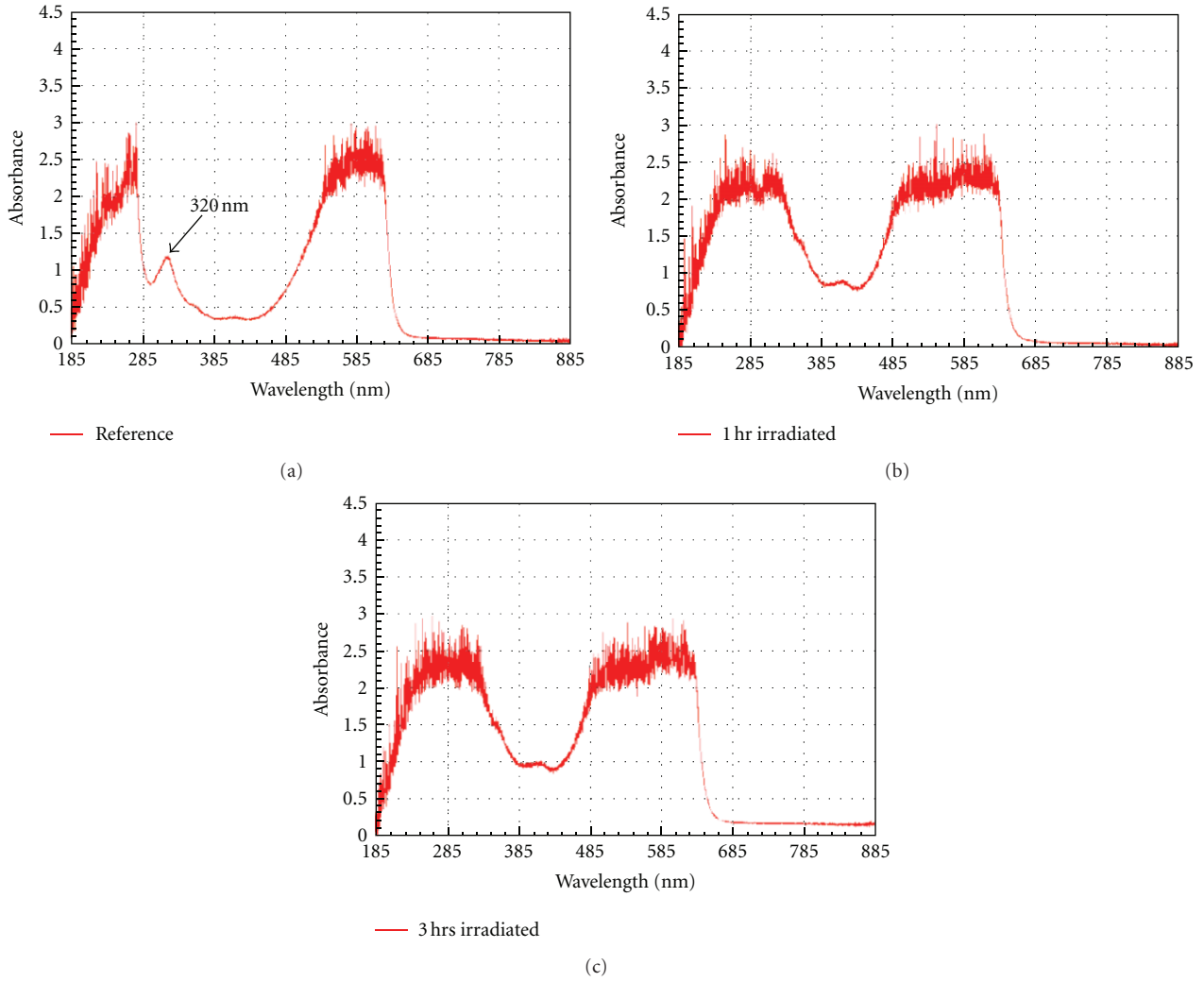


FIGURE 4: Absorption spectra of cresyl violet in ethanol; (a) reference (non-irradiated), (b) 1 hour irradiated, (c) 3 hours irradiated.

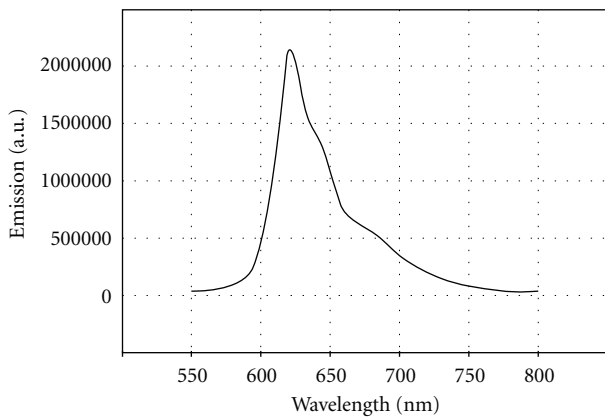


FIGURE 5: Prompt fluorescence spectrum of CV in ethanol.

configuration of the irradiation experiment are illustrated in Figure 2.

In the setup, the sample is placed at distance d (30 cm) away from the phase center of the antenna. The distance d

is adjusted to $2D^2/\lambda > d > kD/2$ where k and λ represent the wavenumber and the wavelength corresponding to 1940 MHz CW frequency, respectively, and D is the maximum antenna dimension. With this distance, the sample remains away from the reactive near field but is at radiative near field (Fresnel region). In Fresnel region, the antenna is not detuned due to the presence of the solution, and most of the transmitted power can be absorbed by the solution. For 925 MHz excitation, the distance d is doubled. With a very crude model, assuming the solution is at far field of the antenna, one can estimate the maximum received power by the solution using Friis equation:

$$\text{Power Transmitted } P_t = 30 \text{ dBm (1 W)}$$

$$\text{Power Density at } d, P_d = \frac{GP_t}{4\pi d^2} \tag{1}$$

$$\text{at } d = 30 \text{ cm, } P_d = 3.29 \text{ W/m}^2$$

$$\text{Received power, } P_r = P_d \sigma = 658 \mu\text{W},$$

assuming 2 cm² incident area. Therefore, 1 hour of irradiation can deliver 2.37 J of energy to the solution, if the solution absorbs all the microwave energy without reflecting any energy back due to mismatch at the interface between the solution and air. If ethanol (relative permittivity $\epsilon_r = 22.55$ [10]) is taken as the dominant dielectric for irradiation experiment, then approximately 57.5% of the energy under normal incidence of electromagnetic wave is absorbed by the solution, that is, 378 μ W of 658 μ W incident power.

3. Results and Discussion

The molecular structure of cresyl violet and cresyl violet perchlorate in solution were planar in the ground state and twisted in the first excited state with exception of amino groups. The delocalization degree is smaller than that of the double bonds in the molecule. Its fluorescence quantum yield appears to be independent of the nature of the solvent, except in water. Its fluorescence quantum yield was determined using conventional colorimetry as well as thermal lens spectrometry and found to be $\phi_F = 0.54 \pm 0.03$. The value for ϕ_F was reported to be independent of concentration [9]. Therefore, cresyl violet was used as fluorescence standard for the concentrations of 10⁻² to 10⁻³ M. In the present study, we tested the concentrations from 10⁻³ to 10⁻⁷ M and found that due to the intramolecular energy hopping of cresyl violet in solution the fluorescence quantum yield was measured as 0.75 ± 0.01 by actinometric measurements. The excitation wavelength was 587 nm, obtained from high-intensity mercury light source. Prompt fluorescence observed at 570–770 nm band with the peak location at 620 nm. Neither Stokes nor anti-Stokes scattering was observed at room temperature experiments. Unfortunately, our experimental setup does not permit us to carry out the same experiments above room temperature, to carry out kinetic measurements. The determined fluorescence lifetime, which is the reorientation time of cresyl violet in ethanol in the S₁ state, was 4.60 ± 0.1 nsec. The magic-angle fluorescence decay curves fit to single-exponential decays.

The amount of thermal energy transferred to the cresyl violet in ethanol due to microwave irradiation is very low compared to the energy required for the transition of electron to a higher vibrational state. However, at each vibrational energy level J_i , there exists many fine rotational bands, as illustrated in Figure 3. For symmetric top molecules having rigid bonds, the energy levels can be determined. More complicated relations are required for elastic bonds [11]. If the molecule is asymmetric top, then it is very difficult to derive an expression for rotational energy bands for each vibrational states due to different moments of inertia about the molecular axis. Thus, measurement of absorbance spectrum is the only viable solution, particularly for cresyl violet.

The ethanol solution act to differentiate the stain, causing myelin and other components to lose color whereas perikarya retain the color. Figure 4 shows the absorption spectrum of nonirradiated cresyl violet in ethanol and the absorption spectra of cresyl violet after one and three hours

of irradiation by microwave. Due to the irradiation by GSM 900/1800 MHz mobile phone frequencies, the absorption band at 320 nm disappeared and a new molecular cresyl violet structure formed. It is also observed that the main absorption bands are broadened and the spectrum showed that the fine structure of the bands appears. Therefore, cresyl violet molecular structure due to the microwave irradiation is changed. The phononic product cannot be used as a laser dye. The prompt fluorescence spectrum of cresyl violet in ethanol solution is shown in Figure 5.

Acknowledgments

This research is partly funded by NATO under Grant no. CRG-950982 and Fulbright Advanced Research Program at Massachusetts Institute of Technology, USA. Fluorescence spectrum and decay time measurements were carried out at UNAM (National Nanotechnology Research Center), Bilkent University, Turkey.

References

- [1] S. J. Isak and E. M. Eyring, "Cresyl violet chemistry and photophysics in various solvents and micelles," *Journal of Photochemistry and Photobiology A*, vol. 64, no. 3, pp. 343–358, 1992.
- [2] P. G. Wolynes, "Dynamics of electrolyte solutions," *Annual Review of Physical Chemistry*, vol. 31, pp. 345–376, 1980.
- [3] I. Rips, J. Klafter, and J. Jortner, "Dynamics of ionic solvation," *The Journal of Chemical Physics*, vol. 88, no. 5, pp. 3246–3252, 1988.
- [4] J. Hubbard and L. Onsager, "Dielectric dispersion and dielectric friction in electrolyte solutions. I," *The Journal of Chemical Physics*, vol. 67, no. 11, pp. 4850–4857, 1977.
- [5] N. Balabai, M. G. Kurnikova, R. D. Coalson, and D. H. Waldeck, "Rotational relaxation of ionic molecules in electrolyte solutions. Anisotropy relaxation and molecular dynamics study," *Journal of the American Chemical Society*, vol. 120, no. 31, pp. 7944–7951, 1998.
- [6] F. Bayrakceken, I. S. Karaaslan, and B. Erol, "Structure elucidation of cresyl violet perchlorate in polyvinylbutyral," *Spectrochim Acta*, vol. 68, pp. 139–142, 2007.
- [7] E. Vogel, A. Gbureck, and W. Kiefer, "Vibrational spectroscopic studies on the dyes cresyl violet and coumarin 152," *Journal of Molecular Structure*, vol. 550–551, pp. 177–190, 2000.
- [8] A. Cavus, M. Wright, J. R. Lombardi, and F. Bayrakceken, "Stark hole-burning spectroscopy of cresylviolet perchlorate in amorphous hosts," *Spectroscopy Letters*, vol. 32, no. 1, pp. 125–137, 1999.
- [9] F. Bayrakceken, I. Karaaslan, K. Yegin, B. Barýs, and M. Bilgic, "Photonic and phononic study of rubrene in solution," *Asian Journal of Spectroscopy*, pp. 119–129, 2010.
- [10] A. Jafari, A. Ghanadzadeh, H. Tajalli, M. Yeganeh, and M. Moghadam, "Electronic absorption spectra of cresyl violet acetate in anisotropic and isotropic solvents," *Spectrochimica Acta A*, vol. 66, no. 3, pp. 717–725, 2007.
- [11] C. H. Townes and A. L. Schawlow, *Microwave Spectroscopy*, Dover, New York, NY, USA, 1975.

Research Article

Optical Energy Transfer Mechanisms: From Naphthalene to Biacetyl in Liquids and from Pyrazine to Biacetyl

Fuat Bayrakceken,¹ Korkut Yegin,² Erdal Korkmaz,³ Yakup Bakis,³ and Bayram Unal³

¹Department of Biomedical Engineering, Yeditepe University, 34755 Istanbul, Turkey

²Department of Electrical and Electronics Engineering, Yeditepe University, 34755 Istanbul, Turkey

³Bionanotechnology Research Center, Fatih University, Istanbul, Turkey

Correspondence should be addressed to Korkut Yegin, kyegin@yeditepe.edu.tr

Received 17 September 2012; Accepted 10 October 2012

Academic Editor: Ipek Karaaslan

Copyright © 2012 Fuat Bayrakceken et al. This is an open access article distributed under the Creative Commons Attribution License, which permits unrestricted use, distribution, and reproduction in any medium, provided the original work is properly cited.

Optical energy transfer from naphthalene to biacetyl in liquids at room temperature is studied. Electronically excited naphthalene with 200–260 nm ultraviolet (UV) light emits photons in its emission band and the emitted photons are absorbed by biacetyl, which, in turn, excites biacetyl phosphorescence. The resulting phosphorescence is very stable with emission peak at 545 nm for different excitation wavelengths from 200 to 260 nm. Similar optical energy transfer is also observed from pyrazine to biacetyl. The sensitization of biacetyl by several aromatic donors has been investigated in detail. An aromatic donor, pyrazine, is raised to its first excited singlet state by absorption of ultraviolet radiation. Excitation wavelengths were selected in the first $n-\pi^*$ band of pyrazine. Intersystem crossing in pyrazine is sufficiently fast to give a triplet yield of almost unity as determined by the biacetyl method. The optical excess energy in the biacetyl will be released as light, which is sensitized fluorescence. Biacetyl is the simplest molecule among a wide range of α -dicarbonyl compounds, which is important for photophysics and photochemistry applications.

1. Introduction

Optical absorption in polar molecules is due to interaction with the permanent dipole moments of individual molecules. The electric field tends to align the dipoles, and the subsequent collision-induced relaxation of the oriented dipoles has a time constant in the picosecond range, giving rise to strong absorption in the far infrared. For nonpolar molecules the much smaller absorption originates in the transient dipole moments induced via collisions in the liquid.

Naphthalene, like many organic compounds, has a conjugated double-bond system, in which every other bond is a double-bond. These conjugated systems have large influence on absorption and emission spectrum of the molecule. Molar absorption coefficient of naphthalene is around 360 and the absorption spectra of naphthalene in rare gas have been extensively studied. The spectra were observed from 333 to 125 nm [1–8]. The transition energies of six transitions were assigned to π -electronic states of naphthalene. Symmetry properties of the first two excited singlet states and

triplet lifetime were also reported in the context of triplet energy transfer [9–18]. Naphthalene in liquid has a different emission spectra than that of vapor phase, in which room temperature transitions are more defined.

Biacetyl, the compound 2,3-butanedione, is the simplest molecule among a wide variety of α -dicarbonyl compounds, which has been the subject of considerable study for photophysics and photochemistry applications. The ground state of biacetyl is known to be Raman-active and IR-active in not only solid but also liquid and vapor phases. The principle absorption bands are due to $n-\pi^*$ electronic transitions [19, 20]. The absorption and emission spectra of the biacetyl crystal exhibit sharp vibrational structure at low temperatures [21].

Triplet-triplet energy transfer from naphthalene to biacetyl in vapor phase has been studied in [22]. In that study, decay times for different mixtures of naphthalene and biacetyl were measured under different biacetyl pressures. It was shown that the fluorescence decay time of naphthalene in cyclohexane was 96 ns [23, 24] and 130 ms lifetime for

triplet state of naphthalene [22]. In this study, we concentrate on the liquid form of naphthalene and biacetyl at room temperatures as this application of the mixture is quite simple and easy to produce. It is observed that the emission spectrum of biacetyl is very stable. This may open new research directions such that incident light energy can be transferred to different wavelengths as in optical mixers and frequency down-conversion devices.

2. Material and Methods

Biacetyl and naphthalene, were of Aldrich reagent grade, used as received without any further purification, and were mixed at atmospheric pressure. The concentration of biacetyl and naphthalene was between 10^{-3} and 10^{-4} M, with the relative concentration of naphthalene/biacetyl 1/2 to 1/3 for best emission. Two Princeton Instruments Acton Advanced SP2300 model monochromators were used for all optical measurements. These devices have 600 g/mm grating with a focal length of 300 mm. The measurement setup is illustrated in Figure 1. A 500 W Xenon bulb was placed in front of the entrance slit of monochromator-1 to obtain maximum amplitude, and the entrance and exit slits were adjusted to 650 μ m openings. A computer-controlled software adjusts monochromatic beams with 200–300 nm wavelength with a 10 nm step and they were emitted from the exit of monochromator-1. A quartz lens was used to focus emitted beam on the sample. The excited sample emitted beam perpendicular to the excitation beam. This emitted beam was focused on the slit of monochromator-2 with the sequential lenses. The alignment was carried out using microstage to obtain the maximum amplitude from the excited beam. The excited beam was scattered from the quartz tube and liquid interface, however the luminescence was due to the entire mixture. Since the focusing was oriented to the center of the liquid mixture, where the luminescence was dense, the excited beam did not reach and interfere with the monochromator-2. Computer-controlled scan has been performed at monochromator-2 between 300–750 nm with a step of 1 nm and 500 ms period. The emitted beam entering through the 650 μ m slit from monochromator-2 was converted to electrical signals by means of the photomultiplier tube (PMT) depending on the emission amplitude. These signals were further recorded digitally in a computer through a data scan software. Dark room was used for all measurements and measurements were performed at room temperature. The emitted beam reaching the PMT was posed with 500 ms period. Because the Xenon bulb was wavelength filtered at 200–260 nm and the PMT was sensitive to the wavelength, a normalization had to be carried out. For that reason, the sample was replaced with a quartz mirror in the measurement setup and the measurement was repeated. The peaks of excitations have been obtained. The maximum amplitude obtained at 220 nm was used to calculate the normalization coefficient for each excitation wavelength. These coefficients, then were multiplied with the entire spectrum to perform the required normalization.

The setup displayed in Figure 1 was also used to study optical energy transfer from pyrazine to biacetyl. Biacetyl and pyrazine, were of Aldrich reagent grade, used as received without any further purification and were mixed at atmospheric pressure. The concentration of biacetyl and pyrazine was between 10^{-3} and 10^{-4} M, with the relative concentration of pyrazine/biacetyl 1/2 for the best emission.

3. Results and Discussion

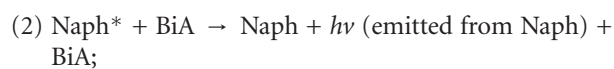
The sensitization of biacetyl fluorescence by naphthalene has been investigated in detail. The emission spectrum of naphthalene-biacetyl is shown in Figure 2, where the mixture is excited from 220 to 260 nm monochromatic source. Peak emission at 545 nm is common to all excitation wavelengths. Side peaks at 491 nm and 610 nm were also observed with relative amplitudes of 0.51 and 0.47 of peak quantum efficiency, respectively. The emission spectrum of the mixture is very stable and common to all excitation wavelengths. Thus, it makes this solution an ideal candidate for photomixing applications.

An aromatic donor is excited to its first excited singlet by absorbing ultraviolet radiation. In addition, the triplet state of the donor molecules are also populated. If an acceptor molecule (i.e., biacetyl) is present, the donor (i.e., naphthalene) can transfer the electronic energy to the acceptor, in which, in turn, the acceptor molecule raises to its lowest triplet state. Excited biacetyl molecules will emit phosphorescence which will be termed as sensitized phosphorescence because the acceptor molecules do not initially absorb incident light. In this study, the donor molecule is naphthalene in liquid and the acceptor molecule is biacetyl in liquid. Hence, the phosphorescence emission of naphthalene will be absorbed by acceptor molecule biacetyl in its triplet state, then excess energy will be emitted as light at different frequencies.

For 200 to 260 nm laser light is absorbed by naphthalene, but at 545 nm, neither naphthalene nor biacetyl absorb light; hence, the system is totally transparent for 545 nm emission line. The optical pumping at 200 to 260 nm excites naphthalene molecules to their first excited singlet level, then excited naphthalene molecules decay back to ground state by fluorescence emission of naphthalene where this emission band of naphthalene coincides with the excitation band of biacetyl. Therefore, the biacetyl molecules will be electronically excited by naphthalene. Excited biacetyl molecules will return to their ground state by fluorescence and phosphorescence emissions. This process is depicted in the following scheme which is summarizing naphthalene and biacetyl interaction :



Naphthalene (Naph) absorbs 200–260 nm light, but BiA does not absorb this light, hence only Naph is electronically excited and BiA is still in the ground state;



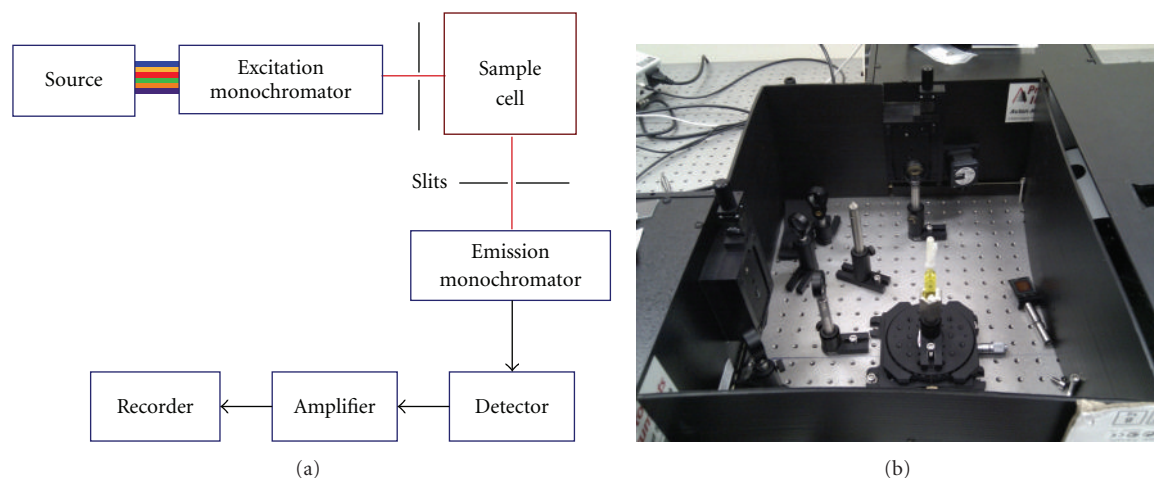


FIGURE 1: Experimental setup, (a) block diagram and (b) part of the actual setup.

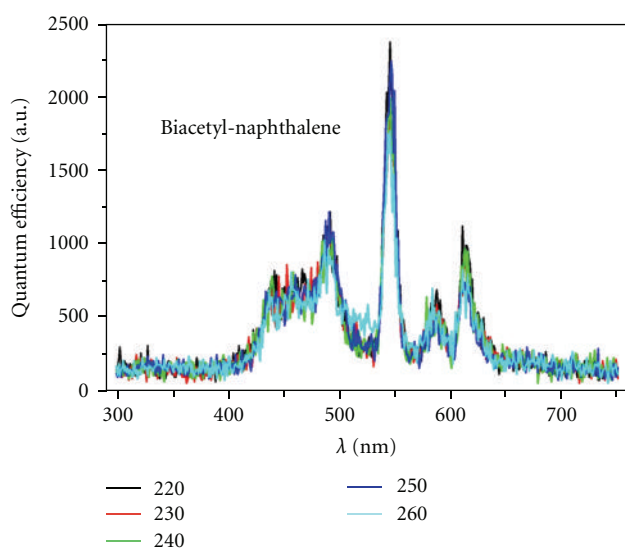
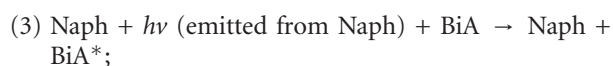
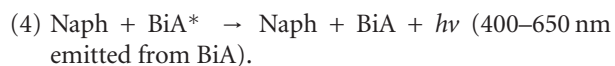


FIGURE 2: Sensitized fluorescence of biacetyl by naphthalene in liquids at room temperature.



BiA* is electronically excited by absorbing the emission of Naph;



The sensitization of biacetyl fluorescence by pyrazine has been investigated in detail, in an attempt to be validated by biacetyl method. Emission spectrum of pyrazine-biacetyl is shown in Figure 3 where the mixture is excited from 305 to 325 nm monochromatic source. Peak emission at 460 nm is common to all excitation wavelengths.

A brief description of the biacetyl methods is as follows. An aromatic donor will be raised to its first excited singlet by absorption of ultraviolet radiation. Among other processes,

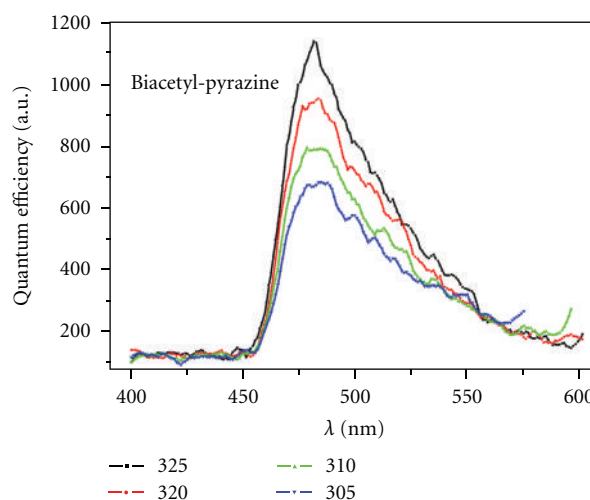
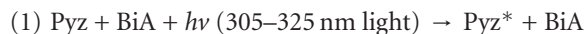


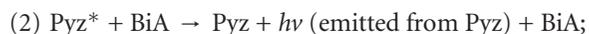
FIGURE 3: Sensitized fluorescence of biacetyl by pyrazine first $\pi\pi$ band.

which will subsequently occur, the triplet state of the donor molecules will also be populated. If a suitable acceptor molecule (i.e., biacetyl) is present, the electronic energy of the donor, pyrazine, can be transferred to the biacetyl producing a biacetyl molecule in its first singlet state. Excited singlet biacetyl molecules so produced will emit fluorescence lights as well as phosphorescence lights. This behavior is labeled as sensitized fluorescence and sensitized phosphorescence, since emissions occur without the emitting molecule initially absorbing light energy. Comparing the quantum yield of the sensitized fluorescence with that produced in a separate experiment, where biacetyl itself is excited affords as determination of the triplet yield of aromatic donor. The triplet yield is, in essence, a measure of the number of singlet donor molecules, which eventually cross over into the triplet manifold. The following reaction mechanism is typical for optical energy transfer from donor to acceptor molecules. Pyrazine emits light as fluorescence and this light

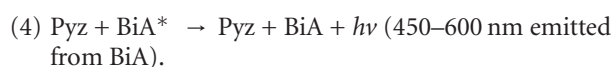
will be absorbed by the acceptor molecule biacetyl, then this optical excess energy in the biacetyl will be released as light, which is sensitized fluorescence. This process is shown in the following scheme which is summarizing pyrazine and biacetyl interaction:



Pyz absorbs 305–325 nm light, but BiA does not absorb this light, hence only Pyz is electronically excited and BiA is still in the ground state;



BiA* is electronically excited by absorbing the emission of Pyz;



4. Conclusions

We show that donor molecule pyrazine emits light and biacetyl absorbs this light as an optical receiver. Similar mechanism is also observed for naphthalene and biacetyl, where donor molecule naphthalene emits light and biacetyl absorbs this light as an optical receiver. Therefore, this mechanism is called an optical antenna at the nanosecond time domain. In our study, neither excimer nor exciplex fluorescence could be recorded.

References

- [1] D. W. Turner, C. Baker, and C. R. Brundle, *Molecular Photoelectron Spectroscopy*, John Wiley & Sons, 1970.
- [2] C. A. Parker, *Photoluminescence of Solutions*, Elsevier, Amsterdam, The Netherlands, 1968.
- [3] J. B. Birks, *Photophysics of Aromatic Molecules*, Wiley-Interscience, London, UK, 1970.
- [4] F. Bayrakceken, "Radiative electronic energy transfer-time studies of naphthalene-biacetyl system by one and two-photon excitation, and optical antenna mechanism," *Spectrochimica Acta Part A*, vol. 61, no. 6, pp. 1069–1074, 2005.
- [5] C. A. Parker and C. G. Hatchard, "Sensitized anti-stokes delayed fluorescence," *Proceedings of the Chemical Society*, pp. 386–387, 1962.
- [6] C. A. Parker and T. A. Joyce, "Phosphorescence of benzophenone in fluid solution," *Chemical Communications*, no. 13, pp. 749–750, 1968.
- [7] J. H. D. Eland and C. J. Danby, "Inner ionization potentials of aromatic compounds," *Zeitschrift Für Naturforschung* 239, p. 355, 1968.
- [8] E. Koch, A. Otto, and K. Radler, "The vacuum ultraviolet spectrum of naphthalene vapour for photon energies from 5 to 30 eV," *Chemical Physics Letters*, vol. 16, no. 1, pp. 131–135, 1972.
- [9] H. W. Offen and D. T. Phillips, "Fluorescence lifetimes of aromatic hydrocarbons under pressure," *The Journal of Chemical Physics*, vol. 49, no. 9, pp. 3995–3997, 1968.
- [10] J. B. Birks, *Organic Molecular Photophysics*, vol. 1-2, John Wiley & Sons, 1973.
- [11] U. Laor and P. K. Ludwig, "Excitation from 3080–2150 Å," *The Journal of Chemical Physics*, vol. 54, no. 3, pp. 1054–1057, 1971.
- [12] T. N. Singh-Rachford, A. Haeefe, R. Ziessel, and F. N. Castellano, "Boron dipyrromethene chromophores: next generation triplet acceptors/annihilators for low power upconversion schemes," *Journal of the American Chemical Society*, vol. 130, no. 48, pp. 16164–16165, 2008.
- [13] E. B. Priestly and A. Haug, "Phosphorescence spectrum of pure crystalline naphthalene," *Journal of Chemical Physics*, vol. 49, no. 2, p. 622, 1968.
- [14] T. N. Singh-Rachford and F. N. Castellano, "Supra-nanosecond dynamics of a red-to-blue photon upconversion system," *Inorganic Chemistry*, vol. 48, no. 6, pp. 2541–2548, 2009.
- [15] P. E. Keivanidis, S. Balushev, T. Miteva et al., "Up-conversion photoluminescence in polyfluorene doped with metal(II)-octaethyl porphyrins," *Advanced Materials*, vol. 15, no. 24, pp. 2095–2098, 2003.
- [16] R. R. Islangulov, D. V. Kozlov, and F. N. Castellano, "Low power upconversion using MLCT sensitizers," *Chemical Communications*, no. 30, pp. 3776–3778, 2005.
- [17] S. Balushev, J. Jacob, Y. S. Avlasevich et al., "Enhanced operational stability of the up-conversion fluorescence in films of palladium-porphyrin end-capped poly(pentaphenylene)," *ChemPhysChem*, vol. 6, no. 7, pp. 1250–1253, 2005.
- [18] S. Balushev, V. Yakutkin, G. Wegner et al., "Two pathways for photon upconversion in model organic compound systems," *Journal of Applied Physics*, vol. 101, no. 2, Article ID 023101, 2007.
- [19] J. C. D. Brand and A. W.-H. Mau, "Low-lying electronic states of biacetyl," *Journal of the American Chemical Society*, vol. 96, no. 14, pp. 4380–4385, 1974.
- [20] J. M. Leclercq, C. Mijoule, and P. Yvan, "Theoretical investigations of excited states of glyoxal and biacetyl," *The Journal of Chemical Physics*, vol. 64, no. 4, pp. 1464–1472, 1976.
- [21] J. W. Sidman and D. S. McClure, "Electronic and vibrational states of biacetyl and biacetyl-d₆," *Journal of the American Chemical Society*, vol. 77, no. 24, pp. 6461–6474, 1955.
- [22] F. Bayrakceken, O. J. Demir, L. Tunçyürek, and I. S. Karaaslan, "Triplet-triplet energy transfer from naphthalene to biacetyl in the vapor phase," *Spectrochimica Acta Part A*, vol. 65, no. 1, pp. 27–31, 2006.
- [23] O. Demir, B. DiBartolo, and F. Bayrakceken, *Bulletin of the American Physical Society*, vol. 26, no. 6, p. 796, 1981.
- [24] Y. Chen, L. Pei, J. Jin, Y. Gao, X. Ma, and C. Chen, "Laser-induced fluorescence spectroscopy of biacetyl A1A_u(S₁)–X1A_g(S₀)," *Chemical Physics Letters*, vol. 323, no. 1-2, pp. 125–129, 2000.

Research Article

Evaluation of Acoustic Cavitation in Terephthalic Acid Solutions Containing Gold Nanoparticles by the Spectrofluorometry Method

Ameneh Sazgarnia¹ and Ahmad Shanei²

¹ Research Center and Department of Medical Physics, School of Medicine, Mashhad University of Medical Sciences, Vakil Abad boulevard, Mashhad 9177948564, Iran

² Department of Medical Physics and Medical Engineering, School of Medicine, Isfahan University of Medical Sciences, Darvazeh Shiraz boulevard, Isfahan 8174673461, Iran

Correspondence should be addressed to Ahmad Shanei, shanei@med.mui.ac.ir

Received 29 April 2012; Revised 30 September 2012; Accepted 7 October 2012

Academic Editor: Korkut Yegin

Copyright © 2012 A. Sazgarnia and A. Shanei. This is an open access article distributed under the Creative Commons Attribution License, which permits unrestricted use, distribution, and reproduction in any medium, provided the original work is properly cited.

Background. When a liquid is irradiated with high intensity and low-frequency ultrasound, acoustic cavitation occurs. The existence of particles in a liquid provides nucleation sites for cavitation bubbles and leads to a decrease in the ultrasonic intensity threshold needed for cavitation onset. **Materials and Methods.** The study was designed to measure hydroxyl radicals in terephthalic acid solutions containing gold nanoparticles in a near field of a 1 MHz sonotherapy probe. The effect of ultrasound irradiation parameters containing mode of sonication and ultrasound intensity in hydroxyl radicals production have been investigated by the spectrofluorometry method. **Results.** Recorded fluorescence signal in terephthalic acid solution containing gold nanoparticles was higher than the terephthalic acid solution without gold nanoparticles. Also, the results showed that any increase in intensity of the sonication would be associated with an increase in the fluorescence intensity. **Conclusion.** Acoustic cavitation in the presence of gold nanoparticles has been introduced as a way for improving therapeutic effects on the tumors in sonodynamic therapy. Also, the terephthalic acid dosimetry is suitable for detecting and quantifying free hydroxyl radicals as a criterion of cavitation production over a certain range of conditions in medical ultrasound fields.

1. Introduction

In recent years the use of low-intensity ultrasound in therapeutic applications has become a developing field. One of the main fields of study is sonodynamic therapy (SDT) [1, 2]. This new method of therapy has great potential because of its relatively easy application [1]. Although the mechanism of low-intensity ultrasound in treating malignant tissues is not well understood, the nonthermal effects of ultrasound, especially cavitation, is considered to be a primary reason for these purposes [3]. Cavitation can occur at stable and transient modes. In stable mode, the bubbles oscillate around an equilibrium radius during a considerable number of acoustic cycles without collapsing. In transient cavitation, bubbles grow rapidly and expand up to several times of their original

size and violently collapse during a single acoustic compression cycle [4]. In fact, during the collapse, very high shear stresses and shock waves are produced. Moreover, very high pressure and temperature at the collapse region can produce free radicals, erosion, emulsification, molecular degradation, and sonoluminescence. This type of cavitation can be fatal to cells and is utilized to destroy cancer tumors [5].

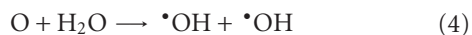
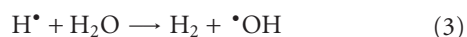
On the basis of a few reports, the existence of a particle in a liquid provides a nucleation site for the cavitation bubble because of its surface roughness and leads to decrease in the cavitation threshold responsible for the increase in the quantity of bubbles, when the liquid is irradiated by ultrasound [6, 7]. Thus, in this context, one approach is based on providing the nucleation sites that participate in

the formation of cavities to reduce the threshold intensity required for cavitation.

Gold nanoparticles (GNPs) have been characterized as novel nanomaterials for use in cancer therapy because of their special optical properties [8, 9]. Their low toxicity, good uptake by mammalian cells, and antiangiogenic properties make GNPs highly attractive for medical applications [10].

In this study, the cavitation potential of GNPs has been studied via chemical dosimetry method [11] at therapeutic intensities of ultrasound.

Acoustic cavitation generates free radicals from the breakdown of water and other molecules. When water is sonicated, OH radicals are formed on thermolysis of H₂O. The initial step in the decomposition of water is the production of hydroxyl and hydrogen radicals. Simplified equations for production of free radicals by collapse of cavitation in water solutions are shown below [12]:



Such chemical products also may be used to measure cavitation activity. It has been shown that terephthalic acid (TA) [benzene-1, 4-dicarboxylic acid] is suitable for detecting and quantifying free hydroxyl radicals generated by the collapse of cavitation bubbles in ultrasound irradiations. During this process, the TA solution as a dosimetric solution reacts with a hydroxyl radical generated through water sonolysis. Therefore, 2-hydroxyterephthalic acid (HTA) is produced which can be detected using fluorescence spectroscopy with excitation and emission wavelengths at 310 and 420 nm, respectively [13].

2. Materials and Methods

2.1. Preparation and Characterization of Gold Nanoparticles. GNPs were synthesized according to standard wet chemical methods using sodium borohydride as a reducing agent [14]. In this experiment, 50 mL of aqueous solution containing 4.3 mg of solid sodium borohydride was added to 100 mL of 100 μM aqueous solution of tetrachloroauric acid under vigorous stirring which was continued overnight. GNPs thus formed were filtered through 0.22 μm filter paper and used for the experiments [14]. TEM revealed that spherical GNPs of approximately 6–8 nm were formed by this method. Size distribution analysis showed that nearly 70% of the particles resided within 5 to 9 nm of size range.

2.2. Ultrasound Generator System. Ultrasound irradiation was conducted with a therapeutic ultrasound unit (215A; coproduct of Novin Medical Engineering Co., Tehran, Iran; and EMS Co., Reading, Berkshire, England) in a continuous mode at a frequency of 1 MHz with a maximum intensity of 2 W/cm² for 3 minutes. Acoustic calibration for the power

of the device was performed in a degassed water tank, using an ultrasound balanced power meter (UPM 2000; Netech Corporation, Grand Rapids, MI) with uncertainty of ± 1 mW. All quoted intensities were spatial average-temporal average (I_{SATA}) in our experiments. An ultrasound transducer with a surface area of 7.0 cm² was horizontally submerged in the bottom of a glass container filled with degassed water.

2.3. Preparation of Terephthalic Acid Solution. The dosimetry solution of TA was prepared according to the standard protocols, containing TA (2 mmol/L, Aldrich) in almost 800 mL deionized water and then treated with 5 mL NaOH (1 M). Ultrasonic irradiation experiments should be carried out in the presence of an alkaline buffer. To increase the pH value of the solution, NaOH was added to it. The solution was stirred for about one hour and kept in a cool and dark place (4°C) to prevent photochemical reactions [12, 13]. A cylindrical chamber was constructed from PVC in order to sonicate the TA solution (5 cm³). The chamber's floor was made from a thin acoustically transparent parafilm layer.

2.4. Experimental Protocol of Chemical Dosimetry. The chamber containing the TA solution was located in a container filled with degassed water in the near field of the probe at 5 mm distance from the surface of the probe. To perform experiments under progressive wave conditions and limit the action of acoustic reflection from the wall of the container, the inner surfaces of the anterior side of the probe was covered by absorbent ultrasound material [12]. The sonication time of the TA solution was selected at 20 min [12]. In such circumstances the maximum increase in temperature was 3°C (18–20°C). The measurements were performed on two TA solutions: TA solution containing GNPs and TA solution without GNPs. After ultrasound exposure at different intensities (0.5, 1 and 2 W/cm²) in continuous and pulsed (in duty cycle of 50%) modes on each solution, its fluorescence signal intensity was recorded using a spectrofluorimeter (FP-6200, Jasco, Japan) with excitation and emission wavelengths at 310 and 420 nm, respectively. The irradiated solutions were kept in a dark place through the experiment and fluorimetric assessments were measured within 2 to 4 hours after sonication. Before ultrasound irradiation, the fluorescence signal of the solutions was also measured. Each experiment was repeated three times.

2.5. Data Analysis. A statistical analysis was performed using SPSS version 13.0 statistical software (SPSS Inc, Chicago, IL). According to the Kolmogorov-Smirnov normality test, the data distribution was normal. Consequently, the paired *t*-test was used to compare the fluorescence signal in two solutions with a confidence level of 95%. The integrated fluorescence signal between different intensities was also compared using one way analysis of variance. Data are presented as Mean \pm SD. *P* < 0.05 was considered as significant.

3. Results

The fluorescence emission spectrum of TA solution without GNPs at 0.5, 1, and 2 W/cm² intensities in continuous mode is shown in Figure 1.

The fluorescence emission spectrum of TA solution containing GNPs at 0.5, 1, and 2 W/cm² intensities in continuous mode is shown in Figure 2.

The results of the fluorescence intensity in the TA solutions in the absence and presence of GNPs at 0.5, 1, and 2 W/cm² intensities in continuous mode are presented in Figure 3.

The fluorescence signal in the TA solution containing GNPs was significantly higher than the TA solution without GNPs in the different intensities in continuous mode ($P < 0.03$).

There was a significant difference in the fluorescence signal intensity in the TA solution containing GNPs among all intensities (0.5, 1 and 2 W/cm²) in continuous mode ($P < 0.05$), but there was no significant difference in the fluorescence intensity in TA solution without GNPs between 1 and 2 W/cm² intensities in continuous mode ($P > 0.3$).

The results of the fluorescence intensity in the TA solutions in the absence and presence of GNPs at 0.5, 1, and 2 W/cm² intensities in pulsed mode (in duty cycle of 50%) are presented in Figure 4.

The fluorescence signal in the TA solution containing GNPs was significantly higher than the TA solution without GNPs at 1 and 2 W/cm² intensities in pulsed mode ($P < 0.05$), but there was no significant difference in the fluorescence signal intensity between TA solution containing GNPs and TA solution without GNPs at 0.5 W/cm² intensity in pulsed mode ($P > 0.06$).

There was a significant difference in the fluorescence signal intensity in the TA solution containing GNPs among all intensities (0.5, 1 and 2 W/cm²) in pulsed mode ($P < 0.04$), but no significant difference in the fluorescence intensity in TA solution without GNPs between 1 and 2 W/cm² intensities in pulsed mode was observed ($P > 0.4$).

Experimental results related to the sonication mode of the TA solutions in the absence and presence of GNPs are shown in Figures 5 and 6.

Data indicated that any increase in intensity of the sonication will be associated with an increase in the fluorescence signal. Also, the recorded fluorescence signal in continuous mode of sonication was higher than the pulsed mode (in duty cycle of 50%) at the same intensity. As seen, the level of fluorescence signal obtained using sonication of the TA solution in the absence and presence of GNPs at 2 W/cm² intensity in continuous mode is significantly higher than the pulsed mode ($P < 0.05$).

4. Discussion

There is considerable interest in the evaluation of cavitation for possibility of SDT which uses low-level ultrasound to release or enhance the action of therapeutic agents *in vivo* [1]. In order to quantify cavitation, certain methods are necessary, which are widely applicable methods. Existing

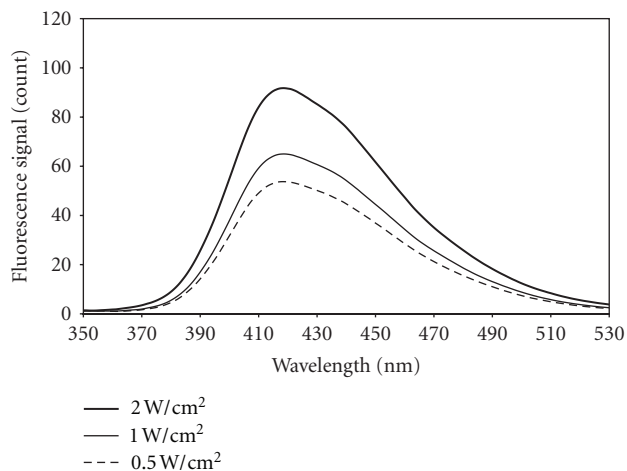


FIGURE 1: Recorded fluorescence emission spectrum from the TA solution without GNPs in the field of 1 MHz ultrasound waves at intensities of 0.5, 1, and 2 W/cm² in continuous mode, excitation wavelength = 310 nm, and emission and excitation band width = 5 nm.

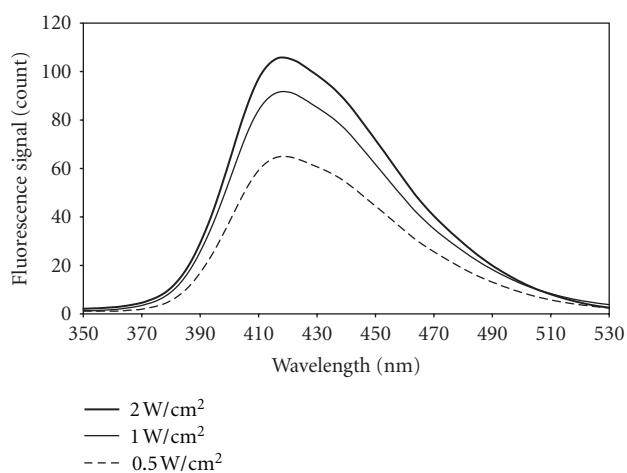


FIGURE 2: Recorded fluorescence emission spectrum from the TA solution containing GNPs in the field of 1 MHz ultrasound waves at intensities of 0.5, 1, and 2 W/cm² in continuous mode, excitation wavelength = 310 nm, and emission and excitation band width = 5 nm.

methods for performing these experiments include acoustic imaging and sonoluminescence whereas other methods such as the electron spin resonance (ESR) and laser holography are difficult and expensive [15]. The ESR is an extremely sensitive method for detecting the radicals produced but its application needs specialist and expensive equipment [15]. Other methods for monitoring the chemical effects of cavitation and free radicals produced are suitable to detect radical species [16]. Currently, cancer-targeted therapy with low-level ultrasound, SDT, has been introduced. The collapse of cavities can produce interesting chemical effects, known as sonochemistry. In order to develop effective SDT, evaluation of effective parameters is the necessary concluding type of ultrasound mode and intensity.

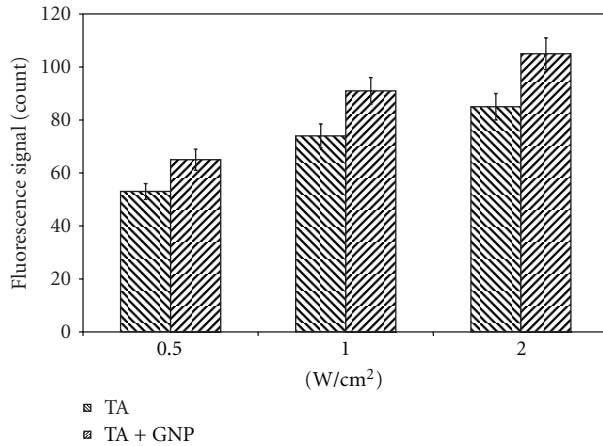


FIGURE 3: Recorded fluorescence signal intensity in the TA solutions in the absence and presence of GNPs at 0.5, 1, and 2 W/cm² intensities in continuous mode, excitation wavelength = 310 nm, and emission and excitation band width = 5 nm.

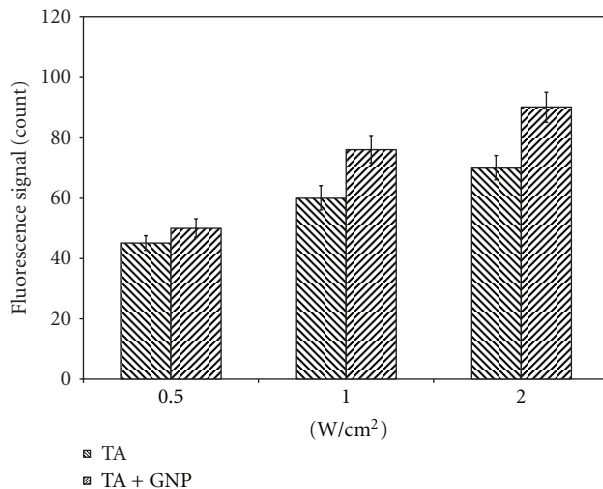


FIGURE 4: Recorded fluorescence signal intensity in the TA solutions in the absence and presence of GNPs at 0.5, 1, and 2 W/cm² intensities in pulsed mode (in duty cycle of 50%), excitation wavelength = 310 nm, and emission and excitation band width = 5 nm.

In this study hydroxyl radical production was measured in the field of 1 MHz ultrasound waves at low-level intensity by the TA dosimetry method. This method of dosimetry is specific for trapping of hydroxyl radical production in fields of ultrasound irradiation, because each molecule of hydroxyl radical is trapped by one molecule of TA and forms one molecule of HTA which can be measured by the fluorescence spectroscopy method. Because this method of dosimetry is based on the fluorimetry method, it is very sensitive for hydroxyl radical measurement.

Barati et al. showed that the TA dosimetry is suitable for detecting and quantifying free hydroxyl radicals as a criterion of cavitation production in medical ultrasound fields [12].

In the present study, we have investigated the cavitation potential of the GNPs by this method.

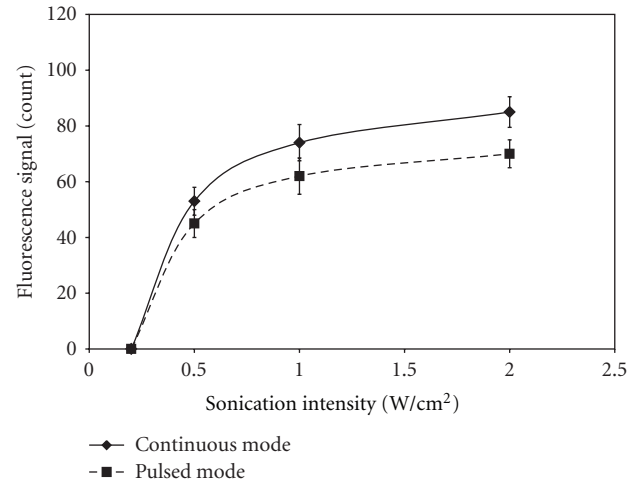


FIGURE 5: Recorded fluorescence signal from the TA solution without gold nanoparticles in the field of 1 MHz ultrasound waves at intensities of 0.5, 1, and 2 W/cm² in continuous and pulsed (in duty cycle of 50%) modes, excitation wavelength = 310 nm, and emission and excitation band width = 5 nm.

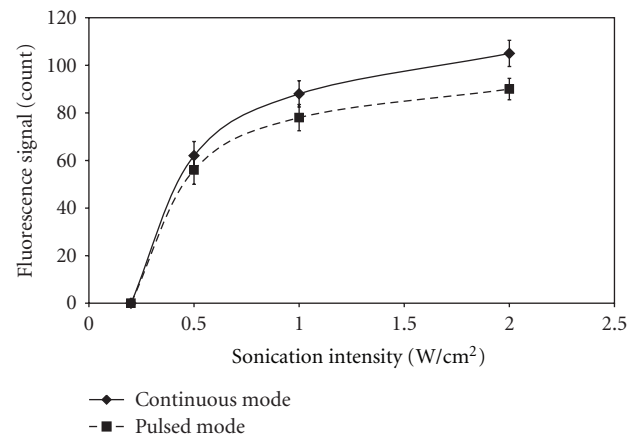


FIGURE 6: Recorded fluorescence signal from the TA solution containing gold nanoparticles in the field of 1 MHz ultrasound waves at intensities of 0.5, 1, and 2 W/cm² in continuous and pulsed (in duty cycle of 50%) modes, excitation wavelength = 310 nm, and emission and excitation band width = 5 nm.

Our results showed that the fluorescence signal intensity for TA solution containing GNPs was higher than the TA solution without GNPs in the different intensities in continuous mode. It should be noted that the above phenomenon is amplified by continuous ultrasound waves with the intensity of 2 W/cm².

This finding could have been related to two courses of action: (1) GNPs acted as cavitation nuclei, that is, the nanoparticles may have acted as the sites for cavitation and increased the cavitation rate [6]; (2) increased collapse of cavities could have been another feasible process.

Consequently, many more OH radicals are created resulting in the higher level of the fluorescence emission.

Therefore, it is predicted that GNPs can increase the cavitation rate in the TA solution containing GNPs.

Tuziuti et al. showed that the existence of particles in a liquid provides a nucleation site for the cavitation bubble due to its surface roughness, and it leads to decrease in the cavitation threshold responsible for the increase in the quantity of bubbles, when the liquid is irradiated by ultrasound [6].

Since SDT is performed in temperatures below the hyperthermia effect threshold on biological environments therefore, in all experiments, temperature changes must be less than 2–3°C.

The results of experiments related to the sonication mode for 1 MHz ultrasound irradiation in the different intensities show that the fluorescence signal in continuous mode of sonication is 20% higher than the pulsed mode in a 50% duty cycle for SDT. This is due to the dosage of energy released by ultrasound irradiation in continuous mode.

The amount of hydroxyl radicals production versus ultrasound intensity show that, with increasing intensity in continuous and pulsed modes, the hydroxyl radical production is increased.

Experimental results obtained by sonication of the TA solutions have indicated that the ultrasound irradiation parameters such as mode of exposure, intensity, and nucleation sites for bubbles generation are effective in hydroxyl radical production and, in turn, in the production of cavitation.

It should be noted that the above phenomenon is amplified by continuous ultrasound waves with the intensity of 2 W/cm².

5. Conclusion

Acoustic cavitation in the presence of GNPs has been introduced as a way for improving therapeutic effects on the tumors in SDT. TA dosimetry is a suitable method for monitoring the acoustic cavitation effects by measurement of hydroxyl radicals in medical ultrasound ranges. It should be remembered, however, that this method employs a chemical dosimeter and as such it may be the only ideal dosimeter for estimation of cavitation production.

References

- [1] T. Yu, Z. Wang, and T. J. Mason, "A review of research into the uses of low level ultrasound in cancer therapy," *Ultrasonics Sonochemistry*, vol. 11, no. 2, pp. 95–103, 2004.
- [2] I. Rosenthal, J. Z. Sostaric, and P. Riesz, "Sonodynamic therapy review of the synergistic effects of drugs and ultrasound," *Ultrasonics Sonochemistry*, vol. 11, no. 6, pp. 349–363, 2004.
- [3] N. Yumita, R. Nishigaki, and S. I. Umemura, "Sonodynamically induced antitumor effect of Photofrin II on colon 26 carcinoma," *Journal of Cancer Research and Clinical Oncology*, vol. 126, no. 10, pp. 601–606, 2000.
- [4] H. Tang, C. C. J. Wang, D. Blankschtein, and R. Langer, "An investigation of the role of cavitation in low-frequency ultrasound-mediated transdermal drug transport," *Pharmaceutical Research*, vol. 19, no. 8, pp. 1160–1169, 2002.
- [5] P. Marmottant and S. Hilgenfeldt, "Controlled vesicle deformation and lysis by single oscillating bubbles," *Nature*, vol. 423, no. 6936, pp. 153–156, 2003.
- [6] T. Tuziuti, K. Yasui, M. Sivakumar, Y. Iida, and N. Miyoshi, "Correlation between acoustic cavitation noise and yield enhancement of sonochemical reaction by particle addition," *Journal of Physical Chemistry A*, vol. 109, no. 21, pp. 4869–4872, 2005.
- [7] C. H. Farny, T. Wu, R. G. Holt, T. W. Murray, and R. A. Roy, "Nucleating cavitation from laser-illuminated nano-particles," *Acoustic Research Letters Online*, vol. 6, no. 3, pp. 138–143, 2005.
- [8] X. Huang, P. K. Jain, I. H. El-Sayed, and M. A. El-Sayed, "Plasmonic photothermal therapy (PPTT) using gold nanoparticles," *Lasers in Medical Science*, vol. 23, no. 3, pp. 217–228, 2008.
- [9] G. F. Paciotti, L. Myer, D. Weinreich et al., "Colloidal gold: a novel nanoparticle vector for tumor directed drug delivery," *Drug Delivery*, vol. 11, no. 3, pp. 169–183, 2004.
- [10] J. C. Y. Kah, M. C. Olivo, C. G. L. Lee, and C. J. R. Sheppard, "Molecular contrast of EGFR expression using gold nanoparticles as a reflectance-based imaging probe," *Molecular and Cellular Probes*, vol. 22, no. 1, pp. 14–23, 2008.
- [11] H. Hasanzadeh, M. Mokhtari-Dizaji, S. Z. Bathaie, and Z. M. Hassan, "Evaluation of correlation between chemical dosimetry and subharmonic spectrum analysis to examine the acoustic cavitation," *Ultrasonics Sonochemistry*, vol. 17, no. 5, pp. 863–869, 2010.
- [12] A. H. Barati, M. Mokhtari-Dizaji, H. Mozdarani, S. Z. Bathaie, and Z. M. Hassan, "Free hydroxyl radical dosimetry by using 1 MHz low level ultrasound waves," *Iranian Journal of Radiation Research*, vol. 3, no. 4, pp. 163–169, 2006.
- [13] C. Haosheng, W. Jiadao, and C. Darong, "Cavitation damages on solid surfaces in suspensions containing spherical and irregular microparticles," *Wear*, vol. 266, no. 1–2, pp. 345–348, 2009.
- [14] R. Bhattacharya, P. Mukherjee, Z. Xiong, A. Atala, S. Soker, and D. Mukhopadhyay, "Gold nanoparticles inhibit VEGF165-induced proliferation of HUVEC cells," *Nano Letters*, vol. 4, no. 12, pp. 2479–2481, 2004.
- [15] G. J. Price, F. A. Duck, M. Digby, W. Holland, and T. Berryman, "Measurement of radical production as a result of cavitation in medical ultrasound fields," *Ultrasonics Sonochemistry*, vol. 4, no. 2, pp. 165–171, 1997.
- [16] T. J. Mason, J. P. Lorimer, D. M. Bates, and Y. Zhao, "Dosimetry in sonochemistry: the use of aqueous terephthalate ion as a fluorescence monitor," *Ultrasonics Sonochemistry*, vol. 1, no. 2, pp. S91–S95, 1994.

Research Article

Detection of Ammonia in Liquids Using Millimeter Wave Spectroscopy

Hilmi Ozturk,¹ Hakki Nazli,¹ Korkut Yegin,² and Mehmet Sezgin¹

¹The Scientific and Technological Research Council of Turkey, Gebze, Kocaeli, Turkey

²Department of Electrical and Electronics Engineering, Yeditepe University, Istanbul, Turkey

Correspondence should be addressed to Hilmi Ozturk, hilmi.ozturk@tubitak.gov.tr

Received 13 July 2012; Accepted 5 October 2012

Academic Editor: Ipek Karaaslan

Copyright © 2012 Hilmi Ozturk et al. This is an open access article distributed under the Creative Commons Attribution License, which permits unrestricted use, distribution, and reproduction in any medium, provided the original work is properly cited.

Detection of ammonia plays a vital role for counter-bioterrorism applications. Using millimeter wave absorption measurements, ammonia dissolved in water solution is analyzed and compared to water-only solution. The inversion of ammonia molecule results in split rotational spectral lines and transitions of these lines can be detected. Two-port measurements were carried out with vector network analyzer and measurements revealed that ammonia presence can be identified, especially between 30–35 GHz.

1. Introduction

Millimeter and submillimeter range of electromagnetic spectrum offer many possibilities for detection and identification of chemical structures. In this range many atoms, molecules and crystals have sharp, strong spectral lines that are very helpful in identifying materials [1]. The principal class of spectra analyzed is the one that arises from the rotation spectra of gaseous molecules. Vibrational spectroscopy of solids and electronic resonances such as plasma oscillations, cyclotron resonance, and paramagnetic resonance can also be observed using this part of the electromagnetic spectrum [2].

Chemical structures exhibit unique absorption and emission spectra at millimeter waves. Emission and absorption lines that arise from particular arrangement of the molecule are mostly attributed to electric dipole moment arrangement of the molecule [3–5]. Especially, spectra of gaseous molecules present fundamental rotational frequencies. On the other hand, transitions between the vibrational states of the molecule are more radiative and these can be observed in the infrared and near infrared of visible region of the spectrum. Lower energy rotational states give rise to emissions at mm-wave region, but are mostly masked by emissions due to molecular interactions. In addition, at atmospheric pressures the mm-wave spectral lines are broadened making them difficult in identification of gaseous molecules.

Ammonia, NH_3 , is an extremely important bulk chemical widely used in fertilizers, plastics, and explosives. Its detection plays a vital role for counter-terrorism measures. Gaseous detection of ammonia using pressurized waveguide section at Ka band was demonstrated in [6]. However, suggested measurement method is somewhat impractical, and the results showed only 0.5 dB attenuation compared to air only mixture. Infrared and Raman spectroscopy of ammonia in liquid [7–14] and detection of ammonia at interstellar space [15] have been analyzed extensively. Our goal in this study is to detect ammonia mixed in water utilizing mm-wave spectroscopy. Instead of passive, active detection method is used and promising results are obtained.

2. Material and Methods

Ammonia mixed in water with 25% concentration, reagent grade, was used as received. The measurement setup is shown in Figure 1. Agilent PNA-X type Network Analyzer was calibrated from 20 to 40 GHz with intermediate frequency at 1 kHz, number of calibration points set to 10,000, and power level to +5 dBm. Network Analyzer as a two-port device can simultaneously measure input reflection and transmission to the other port in terms of Scattering (S) parameters. In this configuration S_{21} represents signal received at port 2 when input signal is applied to port 1, with 50 Ohm port impedance. S_{21} is used as the main data for comparison

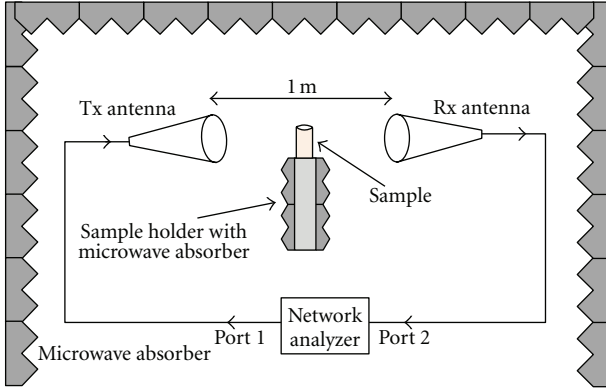


FIGURE 1: Measurement setup for samples.

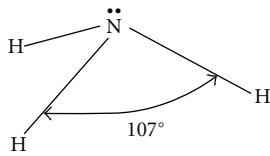


FIGURE 2: Ammonia molecule.

of detection. Wideband conical antennas were used for transmission and reception. Although the antennas were rated from 26.5 to 40 GHz, their port match and gain were found satisfactory starting from 23 GHz. Nevertheless, measurements were carried out relative to water-only sample, and basis of comparison were made with reference to that sample. Measurements were repeated several times to ensure that observed data was stable and not changing with time.

3. Results and Discussion

Ammonia molecule can be described as a near prolate top molecule. NH_3 molecule has a large dipole moment, and its geometry resembles a triangular pyramid as shown in Figure 2.

The electronic arrangement in nitrogen follows the octet rule and the four pairs of electrons (three bonding pairs and one non-bonding pair) repel each other, leading to the molecule's nonplanar geometry. The H–N–H bond angle of 107° is fairly close to the tetrahedral angle of 109.5° . The polarity of NH_3 molecules and their ability to form hydrogen bonds are the main reasons for high solubility of ammonia in water.

The molecular rotation energy of rigid symmetric is given as

$$E = \frac{L_x^2 + L_y^2}{2I_\perp} + \frac{L_z^2}{2I_\parallel}, \quad (1)$$

where angular momentums in respective coordinates are represented as L_x , L_y , and L_z , and the moment of inertia parallel to and perpendicular to z -axis are I_\parallel and I_\perp ,

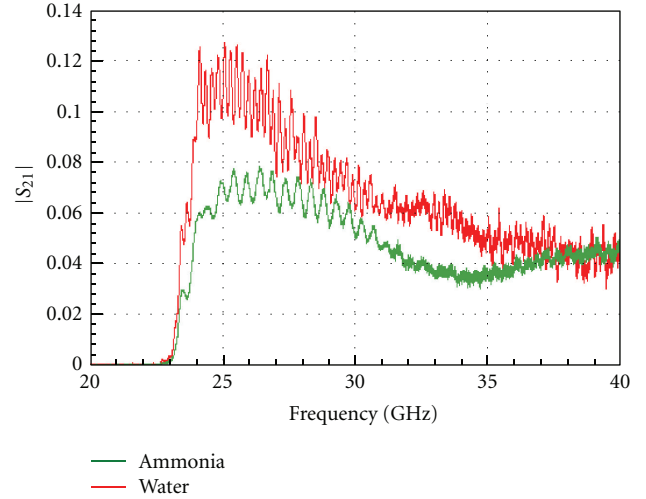


FIGURE 3: Transmission measurements of water-only and water-ammonia liquid solutions.

respectively. This can also be expressed in terms of total angular momentum L , where $L^2 = L_x^2 + L_y^2 + L_z^2$, as follows:

$$E = \frac{L^2}{2I_\perp} + \frac{L_z^2}{2I_\parallel} \left(\frac{1}{I_\parallel} - \frac{1}{I_\perp} \right). \quad (2)$$

The quantum mechanical expression for the energy is obtained by $L^2 = J(J+1)\hbar^2$ and $L_z^2 = K^2\hbar^2$, where $K = 0, \pm 1, \pm 2, \dots, \pm J$ and $J = 0, 1, 2, \dots$. Thus, allowed energy levels can be expressed as

$$\varepsilon_{J,K} = \frac{E_{J,K}}{hc} = \tilde{B}J(J+1) + (\tilde{A} - \tilde{B})K^2, \quad (3)$$

where

$$\tilde{A} = \frac{\hbar}{4\pi c I_\parallel}, \quad \tilde{B} = \frac{\hbar}{4\pi c I_\perp}. \quad (4)$$

The selection rules for rotational spectra of symmetric top molecules are $\Delta J = \pm 1$ and $\Delta K = 0$, that is, the dipole moment of the molecule is oriented along the principal axis and an electromagnetic radiation can not affect the rotation of the molecule about its principal axis. Hence, the rotation is independent of K , and rotational changes about the symmetry axis do not produce rotational spectrum. The inversion of ammonia molecule causes the rotational line to break up and transitions occur between the split levels. The transitionally split energy levels can be approximated by [6]:

$$\varepsilon = \varepsilon_0 + aJ(J+1) + (a-b)K^2, \quad (5)$$

where $\varepsilon_0 = 23.787$, $a = -0.151$, and $(a-b) = 0.211$ GHz. Although approximate, the above equation is used to determine the J - K transition frequencies. Transition frequencies up to 40 GHz are shown in Table 1.

Measurement setup is used for water-only and water-ammonia liquid mixtures. Transmission measurement of S_{21} is recorded for both sample sets. Since the samples are in

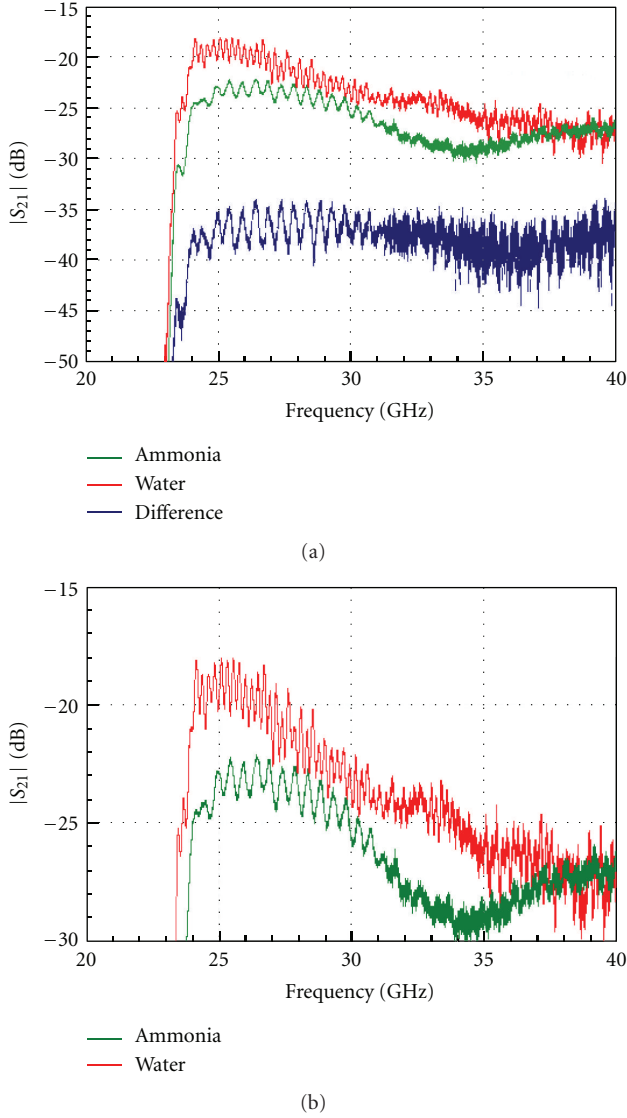


FIGURE 4: Logarithmic scale results of measurements: (a) larger scale with difference; (b) smaller scale for magnitude comparison.

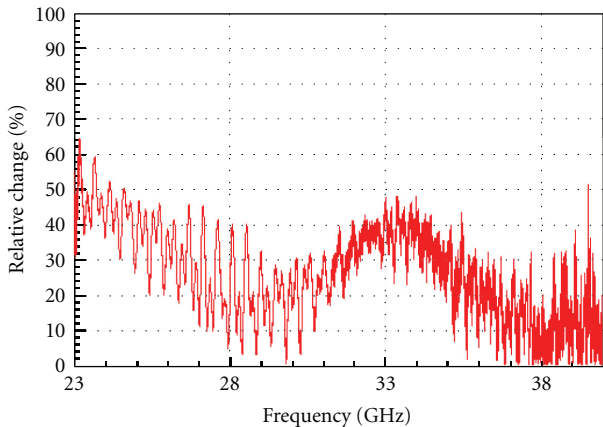


FIGURE 5: Relative percent change of ammonia-water sample with reference to water-only sample.

TABLE 1: NH_3 J - K transitions using approximate formula.

$J(K)-J(K)$	Freq (GHz)
2(1)-2(1)	23.092
8(7)-8(7)	23.254
1(1)-1(1)	23.696
9(8)-9(8)	23.701
3(3)-3(3)	23.874
4(4)-4(4)	24.143
10(9)-10(9)	24.268
5(5)-5(5)	24.532
11(10)-11(10)	24.955
6(6)-6(6)	25.041
7(7)-7(7)	25.67
12(11)-12(11)	25.762
8(8)-8(8)	26.419
13(12)-13(12)	26.689
9(9)-9(9)	27.288
14(13)-14(13)	27.736
10(10)-10(10)	28.277
15(14)-15(14)	28.903
11(11)-11(11)	29.386
16(15)-16(15)	30.19
12(12)-12(12)	30.615
17(16)-17(16)	31.597
13(13)-13(13)	31.964
18(17)-18(17)	33.124
14(14)-14(14)	33.433
19(18)-19(18)	34.771
15(15)-15(15)	32.022
20(19)-20(19)	36.538
16(16)-16(16)	36.731
21(20)-21(20)	38.425
17(17)-17(17)	38.56
18(18)-18(18)	40.509

the far field of receive and transmit antennas, and reflection from the samples are quite close to each other, one can infer absorption of samples directly from transmission measurements. Comparison of transmission measurements for both samples is shown in Figure 3.

It is observed that there is a considerable degradation of ammonia-water solution compared to water-only solution. The measurement result is also expressed in dB scale with $20 \log(S_{21})$ conversion. The logarithmic scale results with larger and smaller scales are shown in Figure 4. The magnitude of difference between the two measurement results is also shown in Figure 4(a).

Especially between 30 and 35 GHz, the presence of ammonia can be easily distinguished, having almost 5 dB more attenuation than water-only solution. According to Table 1, J - K transitions of 18(17)-18(17), 14(14)-14(14), and 19(18)-19(18) fall into that band. We again stress the fact that an approximating function of the energy levels given in (5) was used in the calculation of these transitions in

gaseous ammonia, which would exhibit deviations in liquid ammonia. From 24 to 26.5 GHz, there is also a clear separation between the transmission measurements, however, the antennas are rated starting from 26.5 GHz, thus, we considered this band less reliable compared to 30–35 GHz band.

The relative percent change in received signal with respect to water-only sample is shown in Figure 5. This can be useful for a threshold detector in identifying ammonia presence since ammonia-water mixture has in excess of 25% relative percent change from 30 to 35 GHz.

4. Conclusion

Even though the measurements were carried out at atmospheric pressures and at room temperature, there is a clear difference between water-only and water-ammonia samples. The attenuation of water-ammonia solution is consistently higher than that of water-only solution. Therefore, it is possible to identify ammonia in water using millimeter wave measurements. When mixed with water, individual spectral lines of ammonia cannot be identified, but their effects on the millimeter wave response of the solution can be seen. These measurements reveal that ammonia in water can be distinguished without resorting to special equipment at millimeter waves. The concentration of ammonia in water was really high in our experiments. Although a small contamination of ammonia is a serious health hazard, its transportation in concentrated quantities for bioterrorism can be detected in millimeter wave range. Ammonia presence in air, of course, requires low atmospheric pressures due to broadened spectral lines. However, future research will concentrate on detection of ammonia in air.

References

- [1] M. C. Kemp, "Millimetre wave and terahertz technology for the detection of concealed threats—a review," in *Optics and Photonics for Counterterrorism and Crime Fighting II*, vol. 6402 of *Proceedings of SPIE*, September 2006.
- [2] C. Banwell and E. M. McCash, *Fundamentals of Molecular Spectroscopy*, McGraw, 1994.
- [3] W. Gordy, "Microwave molecular spectra," in *Technique of Organic Chemistry*, A. Weissberger, Ed., vol. 9, Interscience, New York, NY, USA, 1970.
- [4] P. Atkins and J. de Paula, *Physical Chemistry*, W. H. Freeman, 8th edition, 2006.
- [5] R. J. Silbey, R. A. Alberty, and M. G. Bawendi, *Physical Chemistry*, John Wiley & Sons, New Jersey, NJ, USA, 2004.
- [6] M. Szlazak, S. Y. Yam, D. Majstorovic, H. Hansen, and D. Abbott, "Remote gas detection using millimeter-wave spectroscopy for counter bio-terrorism," in *Biomedical Applications of Micro- and Nanoengineering*, vol. 4937 of *Proceedings of SPIE*, pp. 73–83, December 2002.
- [7] A. R. Emery and R. C. Taylor, "Raman spectroscopy in liquid ammonia solutions. Vibrational frequencies and force constants for isotopic species of the borohydride ion having tetrahedral symmetry," *The Journal of Chemical Physics*, vol. 28, no. 6, pp. 1029–1032, 1958.
- [8] J. T. Kindt and C. A. Schmittenmaer, "Far-infrared dielectric properties of polar liquids probed by femtosecond terahertz pulse spectroscopy," *Journal of Physical Chemistry*, vol. 100, no. 24, pp. 10373–10379, 1996.
- [9] T. Ujike and Y. Tominaga, "Raman spectral analysis of liquid ammonia and aqueous solution of ammonia," *Journal of Raman Spectroscopy*, vol. 33, no. 6, pp. 485–493, 2002.
- [10] A. Bromberg, S. Kimel, and A. Ron, "Infrared spectrum of liquid and crystalline ammonia," *Chemical Physics Letters*, vol. 46, no. 2, pp. 262–266, 1977.
- [11] D. J. Gardiner, R. E. Hester, and W. E. L. Grossman, "Ammonia in the liquid state and in solution: a Raman study," *Journal of Raman Spectroscopy*, vol. 1, no. 1, pp. 87–95, 1973.
- [12] J. T. Kindt and C. A. Schmittenmaer, "Far-infrared absorption spectra of water, ammonia, and chloroform calculated from instantaneous normal mode theory," *Journal of Chemical Physics*, vol. 106, no. 11, pp. 4389–4400, 1997.
- [13] C. E. Cleeton and N. H. Williams, "Electromagnetic waves of 1.1 cm wave-length and the absorption spectrum of ammonia," *Physical Review*, vol. 45, no. 4, pp. 234–237, 1934.
- [14] S. G. Kukolich, "Measurement of ammonia hyperfine structure with a two-cavity maser," *Physical Review*, vol. 156, no. 1, pp. 83–92, 1967.
- [15] A. C. Cheung, D. M. Rank, C. H. Townes, D. D. Thornton, and W. J. Welch, "Detection of NH₃ molecules in the interstellar medium by their microwave emission," *Physical Review Letters*, vol. 21, no. 25, pp. 1701–1705, 1968.